REPORT DOCUMENTATION PAGE

AFRL-SR-BL-TR-01-

O161

Public reporting burden for this collection of information is estimated to average 1 hour per response, including the time for reviewing ins
data needed, and completing and reviewing this collection of information. Send comments regarding this burden estimate or any other a
this burden to Department of Defense, Washington Headquarters Services, Directorate for Information Operations and Reports (0704-0'
4302. Respondents should be aware that notwithstanding any other provision of law, no person shall be subject to any penalty for failin;
valid OMB control number. **PLEASE DO NOT RETURN YOUR FORM TO THE ABOVE ADDRESS.**

1. REPORT DATE (DD-MM-YYYY) 02/02/01	2. REPORT TYPE final Technical	3. DATES COVERED (From - To) 15/06/96 to 14/06/00

4. TITLE AND SUBTITLE
DEPSCOR 95 CALIBRATION OF NUCLEAR MONITORING AND DEVELOPMENT

OF REGIONAL VELOCITY STRUCTURE USING UNIQUE SEISMIC DATA

SETS FROM FORMER SOVIET UNION.

5a. CONTRACT NUMBER

5b. GRANT NUMBER
F49620-96-1-0326

5c. PROGRAM ELEMENT NUMBER

6. AUTHOR(S)
Scott B. Smithson

5d. PROJECT NUMBER

5e. TASK NUMBER

5f. WORK UNIT NUMBER

7. PERFORMING ORGANIZATION NAME(S) AND ADDRESS(ES)

University of Wyoming
Contracts & Grants Accounting
P.O. Box 3355
Laramie, WY
82071-3355

8. PERFORMING ORGANIZATION REPORT NUMBER

9. SPONSORING / MONITORING AGENCY NAME(S) AND ADDRESS(ES)
AFOSR/NM
801 North Randolph Street
Room 732
Arlington, VA
22203-1977

10. SPONSOR/MONITOR'S ACRONYM(S)

11. SPONSOR/MONITOR'S REPORT NUMBER(S)

12. DISTRIBUTION / AVAILABILITY STATEMENT

No Limitations

AIR FORCE OFFICE OF SCIENTIFIC RESEARCH (AFOSR)
NOTICE OF TRANSMITTAL DTIC. THIS TECHNICAL REPORT
HAS BEEN REVIEWED AND IS APPROVED FOR PUBLIC RELEASE
LAW AFR 190-12. DISTRIBUTION IS UNLIMITED.

13. SUPPLEMENTARY NOTES

14. ABSTRACT We study long seismic profiles in the Former Soviet Union that are sourced by a number (1-4) of Peaceful Nuclear Explosions (PNE's). These profiles offer explosions in different geologic materials that generate strong seismic waves that propagate through different tectonic provinces, affecting their propagation characteristics. The ultra-long Deep Seismic Sounding (DSS) profile "Quartz' crosses 6 major geologic provinces in Eurasia and is sourced by 3 nuclear (PNE) and 48 chemical explosions. One almost continuous upper mantle boundary occurs at 65 to 80 km depth, and another with an approximately 40-km thick LVZ occurs at 120-140 km depth. The shallow upper mantle blocks and the two extensive interfaces indicate strong upper mantle heterogeneity imaged by this unique profile. Using travel-time modeling techniques, we associate the teleseismic P_n with whispering gallery modes traveling within the top 160 km of the mantle. The long incoherent coda of this phase results from scattering and from reverberations of seismic waves within the crust. We examine the unusually strong and extensive coda of the long-range P_n (interpreted as a whispering-gallery, WG) phase propagating to beyond 3000 km. Such an extensive coda is inherent not only to WG but to all other P-wave phases and can be explained by crustal scattering. The long coda is a result of excitation of short-period scattered waves (P_g, S_g, L_g, R_g) within the crust by the waves incident from the mantle, or, conversely, by generation of mantle phases from crustal guided waves within the source region. Seismic records from nuclear explosions recorded by Deep Seismic Sounding profiles provide valuable information about the propagation of regional and teleseismic S waves and L_g phases across a variety of tectonic structures of Northern Eurasia. The short-period L_g propagates effectively within the Baltic Shield and is strongly attenuated under the West Siberian Basin. We present an evidence for L_g leakage into the uppermost mantle and also propose multicomponent amplitude measurement and noise correction techniques that facilitate and improve the analysis of secondary phases.

15. SUBJECT TERMS
PNE, Lg, Sn, Pn, crustal structure, upper mantle structure

16. SECURITY CLASSIFICATION OF:			17. LIMITATION OF ABSTRACT	18. NUMBER OF PAGES	19a. NAME OF RESPONSIBLE PERSON Scott B. Smithson
a. REPORT unclassified	b. ABSTRACT unclassified	c. THIS PAGE unclassified	UL	68	19b. TELEPHONE NUMBER (include area code) 307-766-5280

Standard Form 298 (Rev. 8-98)
Prescribed by ANSI Std. Z39.18

TABLE OF CONTENTS

1

Executive Summary

We study long seismic profiles in the Former Soviet Union that are sourced by a number (1-4) of Peaceful Nuclear Explosions (PNE's). These profiles offer explosions in different geologic materials that generate strong seismic waves that propagate through different tectonic provinces, affecting their propagation characteristics. The ultra-long Deep Seismic Sounding (DSS) profile "Quartz' crosses 6 major geologic provinces in Eurasia and is sourced by 3 nuclear (PNE) and 48 chemical explosions. High velocity (8.4 km/sec) uppermost mantle is found under the Mezenskaya depression and under the east flank of the Urals. One almost continuous upper mantle boundary occurs at 65 to 80 km depth, and another with an approximately 40-km thick LVZ occurs at 120-140 km depth. The shallow upper mantle blocks and the two extensive interfaces indicate strong upper mantle heterogeneity imaged by this unique profile. Using travel-time modeling techniques, we associate the teleseismic P_n with whispering gallery modes traveling within the top 160 km of the mantle. The long incoherent coda of this phase results from scattering and from reverberations of seismic waves within the crust. We examine the unusually strong and extensive coda of the long-range P_n (interpreted as a whispering-gallery, WG) phase propagating to beyond 3000 km. Such an extensive coda is inherent not only to WG but to all other P-wave phases and can be explained by crustal scattering. The long coda is a result of excitation of short-period scattered waves (P_g, S_g, L_g, R_g) within the crust by the waves incident from the mantle, or, conversely, by generation of mantle phases from crustal guided waves within the source region. Seismic records from nuclear explosions recorded by Deep Seismic Sounding profiles provide valuable information about the propagation of regional and teleseismic S waves and L_g phases across a variety of tectonic structures of Northern Eurasia. Using the data from profile "Quartz", we demonstrate that the short-period L_g propagates effectively within the Baltic Shield and is strongly attenuated under the West Siberian Basin. We present an evidence for L_g leakage into the uppermost mantle and also propose multicomponent amplitude measurement and noise correction techniques that facilitate and improve the analysis of secondary phases.

Personnel Supported

Igor Morozov, Research Scientist
Elena Morozova, Research Scientist
Yuri Ganchine, Graduate Student
Xin Wan, Graduate Student
Jingru Chen, Graduate Student
Erkan Ay, Graduate Student
Jake Deeds, Undergraduate Student
Michael Hogan, Undergraduate Student
Ann Jacobs, Secretary
Allen Tanner, Secretary
James Schatzman, Professor
Scott Smithson, Professor

·CHAPTER 1

OBSERVATION OF L_g AND S WAVE PROPAGATION ALONG THE ULTRA-LONG RANGE PROFILE "QUARTZ", RUSSIA

I. B. MOROZOV, E. A. MOROZOVA, and S. B. SMITHSON
Department of Geology and Geophysics, University of Wyoming
Laramie, WY 82071-3006, USA

1. Abstract

Seismic records from nuclear explosions recorded by Deep Seismic Sounding profiles provide valuable information about the propagation of regional and teleseismic S waves and L_g phases across a variety of tectonic structures of Northern Eurasia. Using the data from profile "Quartz", we demonstrate that the short-period L_g propagates effectively within the Baltic Shield and is strongly attenuated under the West Siberian Basin. We present an evidence for L_g leakage into the uppermost mantle and also propose multicomponent amplitude measurement and noise correction techniques that facilitate and improve the analysis of secondary phases.

2. Introduction

Over many years, Russian Deep Seismic Sounding (DSS) data have been extensively used by many researchers for a detailed analysis of the velocity structure of the crust and uppermost mantle of the northern Eurasia (see [1] and references therein). Most of these studies, however, concentrated on the analysis of the primary P-wave refracted and reflected waves observed within the first 20-40 sec after the first arrivals.

Long listening times of the DSS nuclear explosion (PNE) data (up to 600 sec), however, allow observations of regional and teleseismic S-wave and L_g arrivals, the second of which is particularly important because of its use as the primary seismic nuclear test discriminant. From this perspective, DSS records provide a unique collection of 3-component recordings of the propagation of regional and teleseismic phases from about 60 PNEs across the variety of tectonic structures representing at least 1/10 of the world's land mass.

In this paper, we examine the character of L_g and regional and teleseismic S waves observed in the records of the ultra-long DSS profile "Quartz". For a description of the location of the profile, its acquisition parameters, tectonic structure crossed by the profile, and for an analysis of the crustal and uppermost mantle structure revealed by the profile, we refer the reader to our paper [1] in this volume.

In the following analysis, while focusing our attention on the observational aspects of amplitude measurements, we demonstrate that the observed propagation characteristics

of the L_g phase vary along the profile "Quartz", and they also differ substantially from the character of L_g observed before in the adjacent regions of the Baltic Shield. In an attempt to explain the significantly lower amplitude of L_g observed along the major part of the profile, we propose a mechanism that might be responsible for the leakage of energy out of the L_g window.

3. S and L_g phases in "Quartz" records

PNE records typically exhibit a consistent sequence of primary P-wave refractions and reflections that taken alone or together with the chemical explosion data formed a basis of several 1-D [3] and 2-D [1, 4, 5] interpretations. On the contrary, due to the high
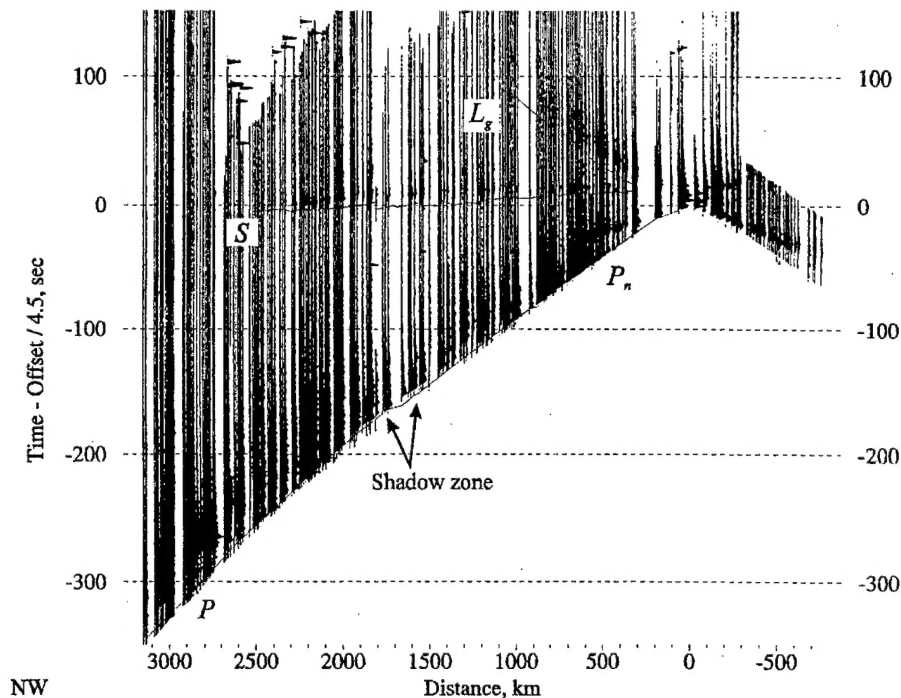

Figure 1. **Trace-normalized three-component vector amplitude records from PNE 323. Reduction velocity is 4.5 km/sec. L_g is strong near 500 km of offset but rapidly loses its energy with distance and nearly disappears after 1200 km. Note the shadow zone between the offsets of 1500 and 1800 km in the first arrivals (indicated by the arrows) and the corresponding gap in the S-wave onset. This shadow zone is caused by a prominent low-velocity zone (LVZ) below a depth of approximately 200 km [3]. Also note the sharp attenuation of S wave amplitude at about 2500 km of offset, apparently corresponding to its attenuation within the LVZ [8].**

level of the crustal reverberations and scattering, even the secondary P-wave phases are typically incoherent and diffuse, leading in some cases to dramatically different interpretations [6-7, 8-9]. Similarly, S- and L_g arrivals are comparatively weak and are masked by the long codas of earlier arrivals. As we will show below, both these features are of primary importance; at the same time, they cause difficulty in displaying these phases in standard record sections. To highlight these weaker phases, and also to pick their onsets, we use 3-component vector amplitude displays [2].

3.1. GENERAL CHARACTER OF S-WAVE AND L_g RECORDS

Figure 1 shows records from the southern "Quartz" PNE 323 (see the map in Figure 1 in [1]). S wave propagates effectively to regional ranges of about 2000 km, after which it becomes much weaker at teleseismic distances, although it still can be distinguished in the records. The shadow zone that was observed in the P-wave onsets between 1500-2000 km and that is caused by the prominent low-velocity zone (LVZ) below 200 km [3] is recognized in the S wave onsets (Figure 1). Compared to L_g and to the background coda of P-wave arrivals, the S wave has a higher frequency content, and it is strongly attenuated after low-pass filtering below about 2 Hz.

The L_g phase from PNE 323 is strong at distances below 500-700 km and at frequencies below 1.5-2 Hz, but is quickly attenuated with distance and nearly disappears between
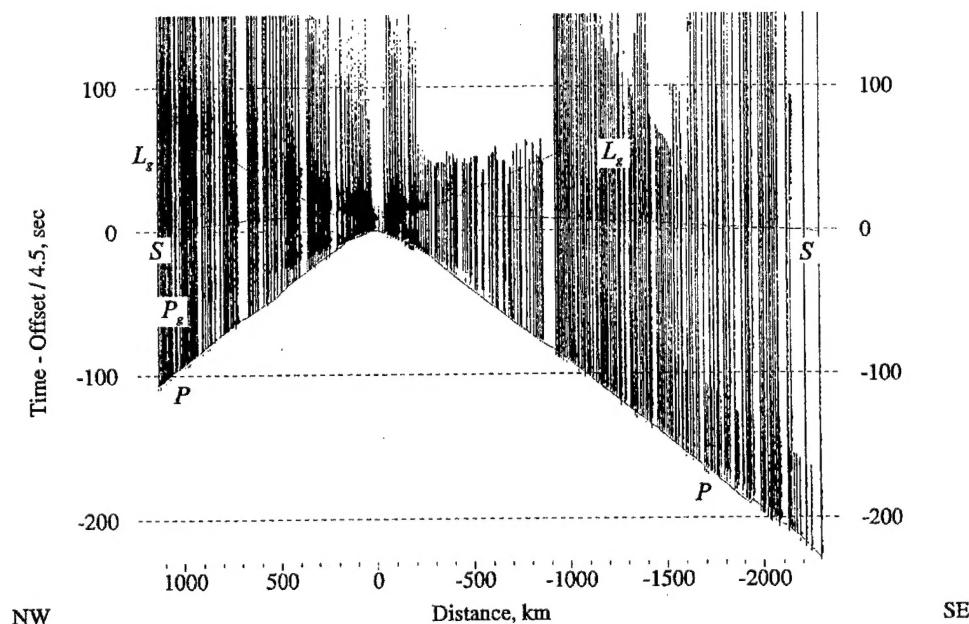
Figure 2. Three-component vector amplitude records from PNE 123 plotted as in Figure 1. Note that the L_g is significantly stronger in the Baltic Shield region, NW of PNE 123.

1200-1400 km from the PNE (Figure 1). Thus in its amplitude-offset dependence, L_g propagation along the West Siberian Basin differs significantly from the propagation within the Baltic Shield where the absolute value of L_g amplitude appears to be substantially stronger, and no indications of its relative attenuation are found, even though the shot point is in a sedimentary basin (Figure 2).

In order to quantify the observed amplitude characteristics of L_g and the regional/teleseismic S waves, it is necessary to account for biases in the estimates caused by the noise background of the phases, and it is also necessary to chose an appropriate amplitude measure. These tasks are performed in the following sections.

3.2. TIME DISTRIBUTION OF RECORDED ENERGY

The S and L_g phases arrive in the background of scattered energy generated by strong P-wave arrivals. As we have observed earlier [9], a dominant part of recorded energy from "Quartz" PNEs propagates above the LVZ at 200 km depth, apparently by means of coupling between the waves scattered within the crust and turning waves in the uppermost mantle. From an observational standpoint, this energy is represented by a long train of energy following the uppermost P-wave mantle phases (Figure 1). This amplitude decay rate is consistent with its interpretation as being due to scattering within the crust, in which crustal S waves and probably L_g waves apparently play a major role [10].

For our interpretation of comparatively quickly decaying L_g, the presence of a strong P-
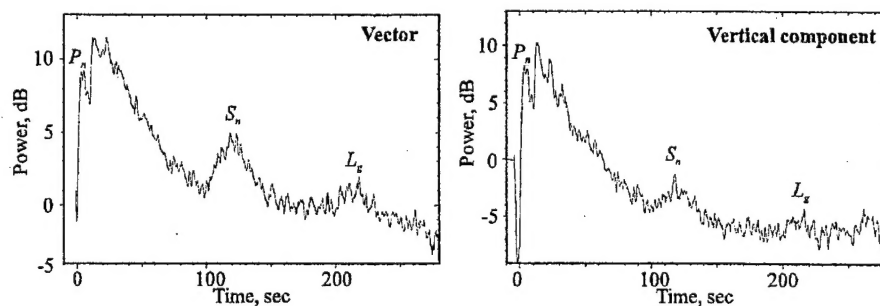
Figure 3. Vector amplitude decay averaged for the records between 1000-1200 km offset. The time window starts at the picked onset of the P_n wave. For a comparison, the plot on the right shows RMS vertical component. Note that along with a somewhat higher stability of the estimates [11], vector measure also provides a more consistent estimate of S_n and L_g amplitude. Note the high energy and long coda of the uppermost mantle refractions and reflections following P_n. This coda forms a strong noise background on which S_n and L_g wave amplitudes are measured.

wave coda may indicate that due to certain features of the velocity structure (e.g., short-scale Moho topography, velocity gradient below the Moho, crustal heterogeneity, basement relief and faulting) the L_g waves traveling within the crust may be strongly coupled to P_n, whispering-gallery modes [9,10] turning within the uppermost mantle and hitting the Moho boundary at grazing angles of incidence. In such a manner, accounting for a faster decay of L_g, this coupling would also enhance the source-induced noise background on which S_n and L_g phases are observed, also leading to their more diffuse character as shown in Figures 1 and 2.

4. Measurement of amplitudes

The amplitudes of P, S, and L_g phases were measured using RMS estimates within carefully chosen time windows picked around the main onsets of the corresponding phases (Figures 1 and 2 show the times of the beginnings of these time gates for PNEs 323 and 123). The lengths of these time gates were generally near 2 sec for P waves, and 10-20 sec for S and L_g waves.

In the measurements of comparatively weak seismic phases arriving on a significant coda background, certain steps need to be taken to enhance the stability and to remove the biases of the estimates. Below we briefly discuss the amplitude measurement techniques employed in our analysis of "Quartz" data.

4.1. THREE-COMPONENT AMPLITUDE MEASURE

As Kennett pointed out in his analysis of L_g propagation along the FENNOLORA profile [11], three-component RMS vector measures result in more stable amplitude estimates than single-component measures. This improvement of stability is apparently due mainly to a partial compensation of scattering effects that result in the rotation of the direction of polarization of particle motion. In our work, we employ an instantaneous vector amplitude measure [2] which has two important advantages over the simple Euclidean RMS measure used in [11]: 1) our measure is instantaneous, providing the maximum possible temporal resolution while being independent of any time windowing; 2) it is accompanied by a set of other instantaneous multicomponent seismic attributes—phase, frequency, polarization vector, ellipticity, etc. We, therefore, routinely use vector amplitude for plotting (see Figures 1 and 2), as well as for amplitude analysis (Figure 3). The advantages of three-component vector measures are illustrated in Figure 3, where the vector amplitude is compared to RMS amplitude of the vertical component of the signal. With smaller scatter of the vector measure, and using all three components, it is possible to detect and correlate weaker arrivals (Figure 3).

4.2. AMPLITUDE CORRECTIONS

Two types of amplitude corrections were applied to the data. First, a correction accounting for the instrument noise was performed according to a noise-adaptive
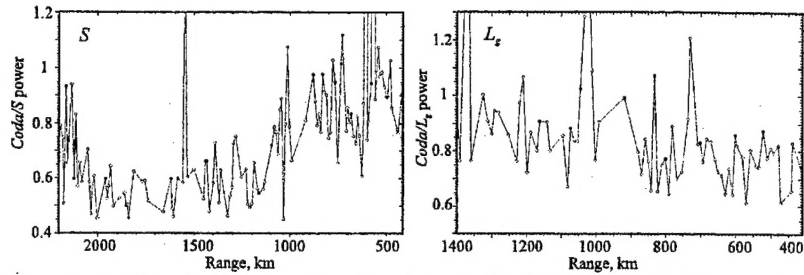
Figure 4. **Estimates of the contribution of the background noise (coda of the previous arrivals) in RMS three-component vector amplitudes of S and L_g arrivals from PNE 323. The background noise levels were measured within 20 sec time windows before the onsets of these arrivals (Figure 1). Note that the noise contribution into the S-wave RMS amplitude increases at near offsets due to the proximity of strong P-wave arrivals; on the contrary, the effect of the noise on L_g amplitude estimates increases with offset because of the attenuation of the L_g wave itself.**

filtering procedure modified after Anderson and McMechan [12]. This procedure reduces "colored" noise in the seismic signal by subtracting a properly scaled instrument noise power spectrum, estimated from the pre-shot noise, from the power spectrum of the signal. As our experience has shown, this correction may be significant for the seismic phases recorded at distances exceeding 1000 km.

The second amplitude correction accounts for the signal-generated noise background on which S- and L_g waves are observed. We estimate these background noise levels by measuring the RMS values of the signal within a 20 sec time window before the onsets of particular phases. The results of these measurements (Figure 4) show that the coda makes a significant and variable with offset contribution to L_g and S-wave amplitudes.

5. Discussion

L_g and S wave amplitude ratio plots (Figure 5) quantitatively illustrate the features of L_g amplitudes observed in Figures 1 and 2. In the West Siberian Basin (NW of PNE 323), where the strongest S wave is generated from a PNE in crystalline rocks of Altay, L_g is strong between 300-700 km, but quickly attenuates with offset, with L_g/S amplitude ratio uniformly decreasing (Figure 5). On the contrary, PNE 123 detonated in Pechora sedimentary basin, generated the strongest L_g in the Baltic Shield region, where L_g/S ratio appears to remain above 1 throughout the available offset range (Figure 5). This observation demonstrates that the characteristics of the Earth's crust along the propagation paths may be critical for observations of L_g phases.

Apparently due to the complexity and interference effects in the P-wave onset, the L_g/P amplitude ratio exhibits large scatter for all three PNEs. This feature appears to be unfortunate for the seismic discrimination applications, where the P/L_g ratio is used as the primary seismic nuclear test discriminant. As we suggested above, the weaker short-period L_g and a complex pattern of the uppermost mantle phases may be due to a common cause—leaking of L_g into the upper mantle. If so, a significantly more detailed understanding of the seismic velocity and attenuation structure of the crust and upper mantle is required in order to be able to derive a robust discrimination criterion.

6. Conclusions

We present the first study of short-period L_g and regional/teleseismic S wave propagation along the DSS profile "Quartz". The following summarizes our findings:

1. instantaneous three-component amplitude measures provide improved estimate stability and quality necessary for a quantitative amplitude analysis of the records,

2. S wave is of a high frequency compared to L_g; there are indications of a S-wave shadow zone corresponding to the LVZ below about 200 km, and the drop in the S-wave amplitude apparently points to high S-wave attenuation within this LVZ, potentially suggesting partial melting within it [13],

3. during its propagation across the West Siberian Basin, L_g quickly decreases in amplitude (faster then the S wave), whereas L_g from a PNE in a sedimentary basin effectively propagates in the Baltic Shield region,

4. although we do not have the sufficient data yet, we speculate that fast dissipation of L_g energy under the West Siberian Basin may be due to its leakage into the mantle through Moho irregularities and crustal heterogeneities; this mechanism may also contribute to the strong coda of the P wave propagation in the uppermost mantle,

5. a better knowledge of the details of deep crustal and upper mantle structures is necessary in order to understand the amplitude characteristics of L_g propagation,

6. short-period P/L_g amplitude ratios obtained for "Quartz" PNEs exhibit poor
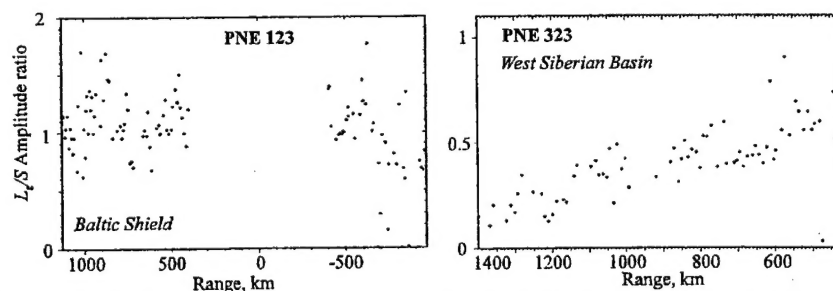
Figure 5. Offset dependence of L_g/S amplitude ratios for PNE 323 and PNE 123. Note the rapid decreasing of L_g/S with distance in the West Siberian Basin (PNE 323), and higher L_g/S within the Baltic Shield (PNE 123 to NW).

stability with offset, making its use as a seismic discriminant problematic.

7. References

1. Morozova, E. A., Morozov, I. B., and Smithson, S. B. Heterogeneity of the uppermost Eurasian mantle along the DSS profile "Quartz", Russia, *this volume.*

2. Morozov, I. B., and Smithson, S. B. (1996) Instantaneous polarization attributes and directional filtering, *Geophysics,* **61**, 872-881.

3. Mechie, J., Egorkin, A. V., Fuchs, K., Ryberg, T., Solodilov, L., and Wenzel, F. (1993) P-wave velocity structure beneath northern Eurasia from long-range recordings along the profile Quartz, *Phys. Earth Planet* Inter., **79**, 269-286.

4. Ryberg, T., Wenzel, F., Mechie, J., Egorkin, A., Fuchs, K., and Solodilov, l. (1996) Two-dimensional velocity structure beneath Northern Eurasia derived from the super long-range seismic profile Quartz, *Bull. Seismol. Soc. Am.,* **86**, 857-867.

5. Schueller, W., Morozov, I. B., and Smithson, S. B. (1997) Crustal and uppermost mantle velocity structure of northern Eurasia along the profile Quartz, *Bull. Seismol. Soc. Am.,* **87**, 414-426.

6. Ryberg, T., Fuchs, K., Egorkin, A. V., and Solodilov, L. (1995) Observations of high-frequency teleseismic P_n on the long-range Quartz profile across northern Eurasia, *J. Geophys. Res.,* 100, 18151-18163.

7. Tittgemeyer, M., Wenzel, F., Fuchs, K., and Ryberg, T. (1996) Wave propagation in a multiple-scattering upper mantle—observations and modeling, *Geophys. J. Int.,* 127, 492-502.

8. Morozov, I. B., Morozova, E. A., and Smithson, S. B. On the nature of the teleseismic P_n phase observed in the recordings from the ultra-long range profile "Quartz", Russia, submitted to *Bull. Seismol. Soc. Am.*

9. Morozov, I. B., Morozova, E. A., and Smithson, S. B. Whispering gallery waves from nuclear explosions of the long-range profile QUARTZ, Russian Eurasia, submitted to *Geophys. Res. Lett.*

10. Dainty, A. M., and Schultz, C. A. (1995) Crustal reflections and the nature of regional P coda, *Bull. Seismol. Soc. Am.,* **85**, 851-858.

11. Kennett, B. L. N. (1993) The distance dependence of regional phase discriminants, *Bull. Seismol. Soc. Am.,* **83**, 1155-1166.

12. Anderson, R. G., and McMechan, G. A., (1988) Noise-adaptive filtering of seismic shot records, *Geophysics,* **53**, no. 5, p. 638-649.

13. Anderson, D. L. (1989) *Theory of the Earth,* Blackwell Scientific Publications, Boston.

CHAPTER 2

HETEROGENEITY OF THE UPPERMOST EURASIAN MANTLE ALONG THE DSS PROFILE "QUARTZ", RUSSIA

E. A. MOROZOVA, I. B. MOROZOV and S. B. SMITHSON
Department of Geology and Geophysics, University of Wyoming
Laramie, WY 82071-3006, USA

1. Abstract

The ultra-long Deep Seismic Sounding (DSS) profile "Quartz' crosses 6 major geologic provinces in Eurasia and is sourced by 3 nuclear (PNE) and 48 chemical explosions. Our interpretation shows a 42-km thick, high-velocity crust under the Baltic Shield, a 29-km thick crust and high-velocity upper mantle under the Mezenskaya depression, 52-km thick crust with high-velocity lower crust and uppermost mantle under the Urals, and 40-km thick crust under the West Siberian Basin deepening to 45 km under the Altay-Sayan fold belt. High velocity (8.4 km/sec) uppermost mantle is found under the Mezenskaya depression and under the east flank of the Urals. One almost continuous upper mantle boundary occurs at 65 to 80 km depth, and another with an approximately 40-km thick LVZ occurs at 120-140 km depth. The shallow upper mantle blocks and the two extensive interfaces indicate strong upper mantle heterogeneity imaged by this unique profile.

2. Introduction

The ultra-long DSS profile "Quartz" which crosses 6 major geologic provinces in Eurasia and is sourced by 3 nuclear explosions and 48 chemical explosions, provides unusually detailed and continuous coverage of the uppermost mantle. The 3850-km-long profile is recorded by 400 3-component recorders at a nominal spacing of 10 km and shows good energy out to more than 3100 km from nuclear explosions (PNEs) and 600 km from chemical explosions (Figure 6). This data is unique in the length of continuous profiling, the number of source points, and in the recording in two directions from each source point. The profile has been interpreted by various groups for either crustal structure using chemical explosions [1-2,3] or upper mantle structure using only nuclear explosions [4, 5]. A review of interpretations of "Quartz" and other DSS profile can be found in [6]. Here we present a combined interpretation of both nuclear and chemical explosions using both first and second arrivals for the detailed structure of the uppermost mantle after taking into account the effect of crustal structure. Interpretation is carried out with the ray tracing modeling program by Zelt and Smith [7]. We will show that velocity structure of the uppermost mantle is affected by travel time anomalies in the crust as determined from chemical explosions, and importantly, uppermost mantle velocity is also determined from these chemical explosions complimented by PNEs for greater detail than can be determined from one source alone.

2. The Data

The profile extends from the Baltic Shield on the NW across the Ural Mountains to the Altay Mountains on the SE (Figure 1). The geologic provinces crossed from NW to SE include the Baltic Shield, Mezenskaya depression, Timan belt, Pechora Basin, Ural Mountains, West Siberian Basin, and Altay-Sayan fold belt (Figure 1). The PNEs are located in the Pechora Basin, the West Siberian Basin and the Altay Mountains (Figure 1).

48 chemical shots were spaced at about 80 km along 3850 km of profile. Two unique aspects of the profile are: 1) continuous profiling of the crust and uppermost mantle over such a great distance, 2) crustal refraction/reflection profiles that are recorded in two directions from each shot point, thus providing empirical

Figure 6. **Map of the western part of the former USSR showing the location of profile "Quartz" and its three PNEs. Major tectonic provinces are indicated.**

evidence of crustal and Moho changes in opposite directions around each shot point. The chemical explosions are recorded into the same receivers on the ground as the nuclear explosions. In contrast with earlier approaches [1-2], we did not velocity filter the data because the station spacing leads to severe aliasing. Travel-time curves from chemical explosions along the entire profile, show good coverage of the Moho from P_mP which generally stays around 8s reduced time corresponding to a depth of about 40 km. Deviations from this time occur in the Mezenskaya depression, Urals, and Altay-Sayan Belt. The chemical recordings typically show P_g, one or two deep crustal refractions and reflections, P_mP and some P_n arrivals (Figure 2). An upper mantle event, P_N, may also be observed (Figure 2). The crustal-uppermost mantle structure is further constrained by data from the PNEs.

The Baltic Shield is characterized by high-velocity (7.2 - 7.4 km/s) lower crust indicated by a high-velocity first arrival and the P_mP asymptote as well as from an earlier tomographic study [3], and crustal thickness is about 42 km. The Mezenskaya depression is marked by sharp, local advances in travel time for P_mP (Figure 2, shot point 77) and for first arrivals from PNE 123 (Figure 3). Both forward and reversed shots show P_n at 6 s reduced time versus 8 s for adjacent crust (Figure 2). Our model accounts for this with a Moho uplift to 29 km depth under the Mezenskaya depression
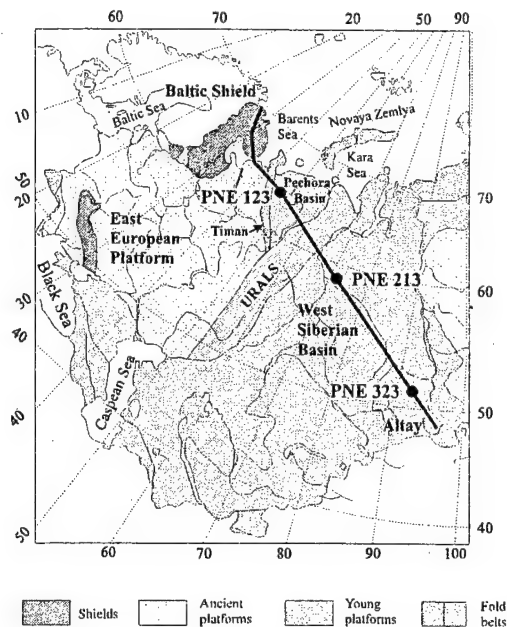
and an upper mantle velocity increase to 8.4 km/s, which is necessary to explain the travel-time advance in the refracted wave from PNE 123 (Figure 3). The modeling shows that the travel-time curves simply cannot be fit with only an uplift in the Moho. A large gravity high occurs over the Mezenskaya depression confirming the seismic interpretation. Based on P_mP, the Moho depth is 39 km under the Timan belt and 33 km under the Pechora Basin (Figure 4).

For the Ural Mountains, chemical shots and PNE 123 show a lower crustal refraction with a velocity of 7.1 km/s (Figure 2, shot point 142, and Figure 3, top) and P_mP from PNE 123 (Figure 3) has a distinctly longer reduced travel time of 8.5 s under the Urals compared with P_mP to the NW under Pechora Basin. Upper mantle refracted arrivals from PNE 213 have a broad travel-time advance just east of the Urals and a sharp local anomaly on the east flank of the Urals (Figure 3, PNE 213). Also, P_n from PNE 123 appears to be blocked by the Urals, and first arrivals at 300 to 800 km offset to the SE are P_N—a reflection from the upper mantle (Figure 3). These data are interpreted as a rather thick 52-km deep root particularly characterized by high velocities up to 7.9 km/ in the lowermost crust and 8.4 km/s in the uppermost mantle, implying that a large amount of anomalously high-velocity material must be present under the east flank of the Urals. The Urals have a 30-km thick, high-velocity lower crust with a 14 km root.

In the West Siberian Basin, P_mP travel-times are almost constant (Figure 2, shot point 277), and no travel-time anomalies are observed in first arrivals from PNEs. Crustal thickness is constant around 41 km. In the Altay-Sayan belt, P_mP travel-time increases and crustal thickness is greater—about 45 km.

A major uppermost mantle reflection, P_N, is traced semi-continuously across the entire profile. This reflection is recorded on 10 chemical shots (Figure 2) and all 3 PNEs (Figure 3). Although the reflection is not followed continuously (Figure 4), we correlate it from record to record at a depth of about 65-80 km. To the south of PNE 123, the first arrival from 300 to 850 km offset is correlated as a reflection from the P_N interface on the basis of its move-out (Figure 3). The depth of this boundary and the mantle velocity above it are influenced by high-velocity lower crust and upper mantle under the Urals. Here our interpretation differs from that of Mechie et at. [4] and Ryberg et al. [5], who interpreted the same event as a uppermost mantle refraction at offsets from 500 to 850 km ignoring the kinematics of this event at shorter offsets. P_n is not seen under the Urals and appears to be blocked by them.

14

When we include events from the PNEs in the crustal/uppermost mantle interpretation, one or two relatively local low-velocity zones are interpreted in the northern part of the profile recorded from PNE 123. We see no evidence for these in the travel-time curves from the two PNEs to the south of the Urals. The NW leg recorded from PNE 123 (Figure 3) shows a large travel time advance over the Mezenskaya depression in the mantle refractions, a P_n event, a P_N from about 60 km depth and two deeper upper mantle arrivals at offsets of 700 to 1000 km. Beyond 900 km, a step in the
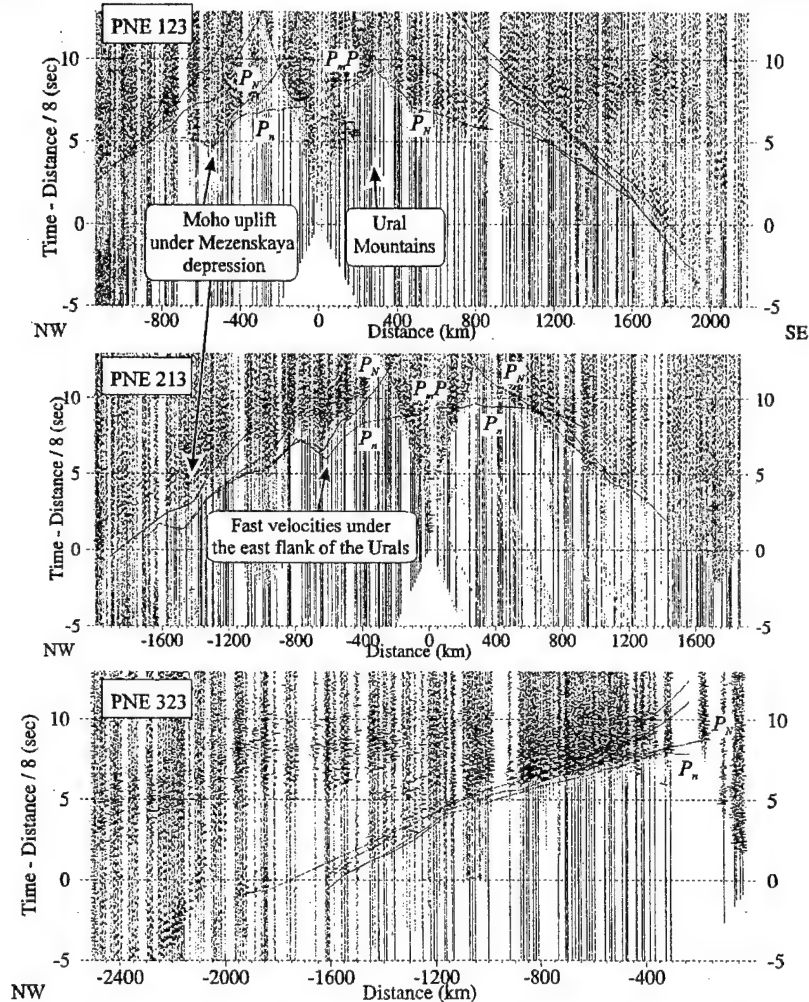
Figure 3. Vertical component records from "Quartz" PNEs showing travel times calculated using our final velocity model (Figure 4). Prominent features of the crustal and Moho structure constrained by these records are indicated. Note that the P_n arrival SW from PNE 123 is blocked by the Urals and the reflection from the 70-km discontinuity (P_N) is observed in the first arrivals to the offsets of 900 km.

first arrival indicates presence of a major low velocity zone in the uppermost mantle. The major LVZ begins at 120 to 140 km depth and extends to about 170 km based on a small velocity decrease.

From PNE 213 to the NW, (Figure 3) P_n is present as a first arrival and shows a strong advance in travel time under the Urals and under the Mezenskaya depression, indicating high velocities in the crust and uppermost mantle of both areas. A P_N arrival resembles that from PNE 123 to the SE. The P_mP travel time branches are essentially the same in both directions from the shot point suggesting similar crustal structures. To the SE, the P_n arrival is very weak, and P_N is followed by a somewhat deeper mantle event refracted under the 70 km depth boundary, indicating the same mantle interface under the West Siberian Basin (Figure 4).

PNE 323 (Figure 3) shows a P_n event to the north followed immediately by a short reflection from 65 km depth interphase and then by a long phase refracted under this boundary. The first arrival from 850 to 1600 km from two branches with apparent velocities of 8.5 and 8.7 km/s, respectively.

3. Discussion and Conclusions

Our crustal and uppermost mantle model (Figure 4) is simpler than previously published versions [1-2] because we did not use a velocity filter and interpreted only the more clear events. In addition we used arrivals from PNEs to constrain our crustal model and secondary arrivals (reflections) to determine uppermost mantle structure.

Under the Baltic Shield, the crust is forty-two kilometer thick and contains high velocity (7.1 km/s) lower crust similar to the earlier results [1-2] and to a recent tomographic study [3]. The thinnest crust (29 km) along the profile occurs under the Mezenskaya depression, which is underlain by high velocity (8.4 km/s) uppermost mantle. Under the Urals, both chemical shot 142 (Figure 2) and PNE 123 (Figure 3) show a lower crustal refraction with an apparent velocity of 7.1 km/s, and also the reflection from PNE 123 (Figure 3) clearly indicates a root under the Urals, which extends to about 52 km depth. A thick, high-velocity lower crust is modeled here underlain by high-velocity upper mantle on the eastern flank of the Urals. Although the exact position of the Moho boundary can vary somewhat, the presence of much high-velocity material in the lower crust and uppermost mantle is required by the strong traveltime advance in the mantle refraction from PNE 213 (Figure 3) and by a gravity anomaly. From an about 40-km thick crust under the West Siberian Basin, the crust thickens to about 45 km under the Altay-Sayan fold belt.

An uppermost mantle boundary at 65 to 80 km depth is traced almost continuously across the profile using reflections and refractions from both chemical and nuclear explosions (Figure 4). We interpret these results as a continuous boundary. The two local LVZs at about 70 km depth may be a function of abnormally high velocities under

the Mezenskaya depression and Ural Mountains. Another major heterogeneity of the upper mantle is a LVZ varying between 120 and 140 km depth with a thickness of about 40 km; this zone has been pointed out by a number of workers [4, 5, 8].

The differences between our interpretation and earlier interpretations [1-2, 5] are caused by our determination of high velocity blocks beneath the Moho based on combined analysis of chemical and nuclear shots and our use of second arrivals and our interpretation of some first arrivals as post-critical reflections (Figure 3). In conclusion, use of numerous shot points over a 3800 km seismic profile reveals significant heterogeneity in the uppermost mantle, in the form of several apparently continuous layers and also blocks of contrasting velocities.

4. References

1. Egorkin, A. V. (1991) Crustal structure from seismic long-range profiles; in V. V. Belousov, N. I. Pavlenkova, and G. N. Kvjatkovskaja (eds.), *Deep Structure of the USSR Territory*, Nauka, Moscow, 118-135 (in Russian).
2. Egorkin, A. V. and Mikhaltsev A.V. (1990) The Results of Seismic Investigations along Geotraverses, in Super-Deep Continental Drilling and Deep Geophysical Sounding, K. Fuchs, Y. A. Kozlovsky, A. I. Krivtsov and M. D. Zoback (Editors), Super-Deep Continental Drilling and Deep Geophysical Sounding, Springer, Berlin, 111-119.
3. Schueller, W., Morozov, I. B., and Smithson, S. B. (1997) Crustal and uppermost mantle velocity structure of northern Eurasia along the profile Quartz, *Bull. Seismol. Soc. Am.,* **87**, 414-426.
4. Mechie, J., Egorkin, A. V., Fuchs, K., Ryberg, T., Solodilov, L., and Wenzel, F. (1993) P-wave velocity structure beneath northern Eurasia from long-range recordings along the profile Quartz, *Phys. Earth Planet* Inter., **79**, 269-286.
5. Ryberg, T., Wenzel, F., Mechie, J., Egorkin, A., Fuchs, K., and Solodilov, I. (1996) Two-dimensional velocity structure beneath Northern Eurasia derived from the super long-range seismic profile Quartz, *Bull. Seismol. Soc. Am.,* **86**, 857-867.
6. Pavlenkova, N. I. (1996) Crust and upper mantle structure in northern Eurasia from seismic data, *Advances in Geophysics*, **97**, 1-133.
7. Zelt C.A. and Smith R.B. (1992) Seismic Traveltime Inversion for 2-D Crustal Velocity Structure, Geoph. Journal International, **108**, 16-34.
8. Thybo H. and Perchuc E (1997) The seismic 8 Discontinuity and Partial Melting in Continental Mantle, Science, **275**, 1626-1629.
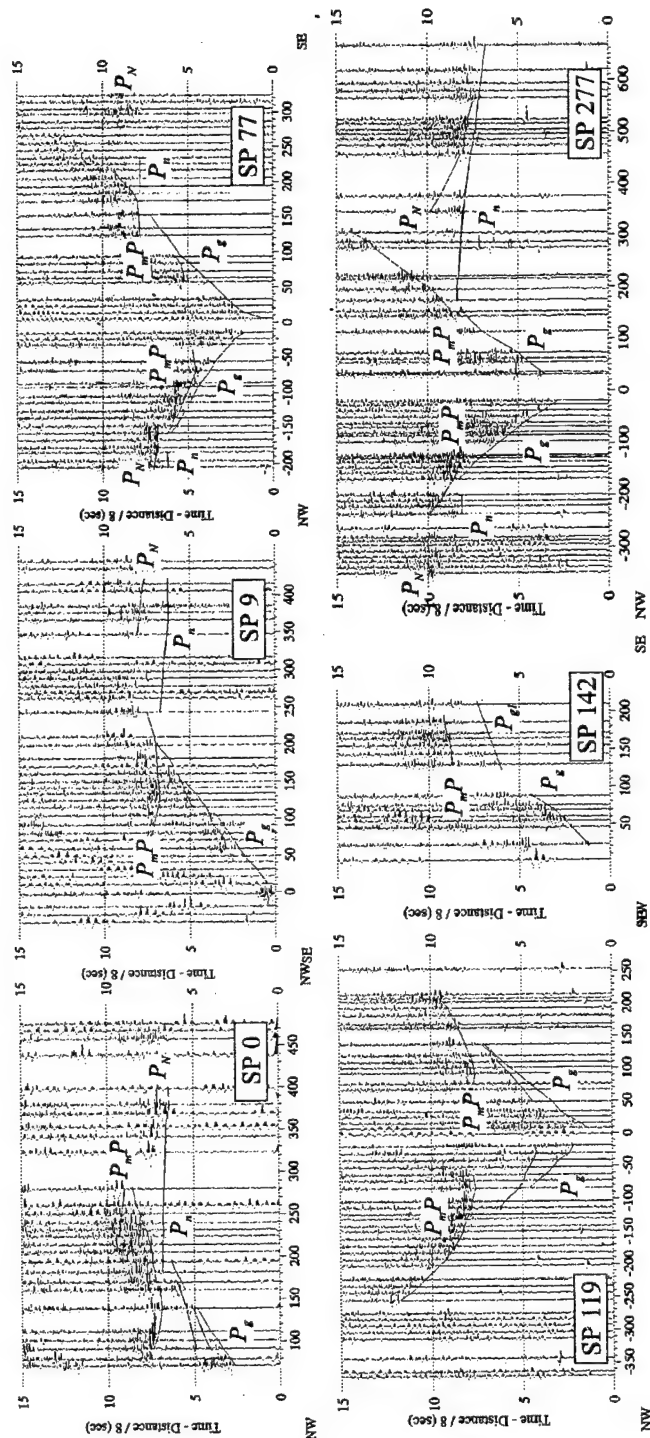
Figure 2. Vertical component record sections from 6 chemical explosions along the profile "Quartz" showing the major phases and corresponding traveltime picks. Most records show sequences of 1-2 crustal reflections following in time P_g travel time curves (not labeled). Note consistent reflections from the depth of about 70 km, labeled as P_N.
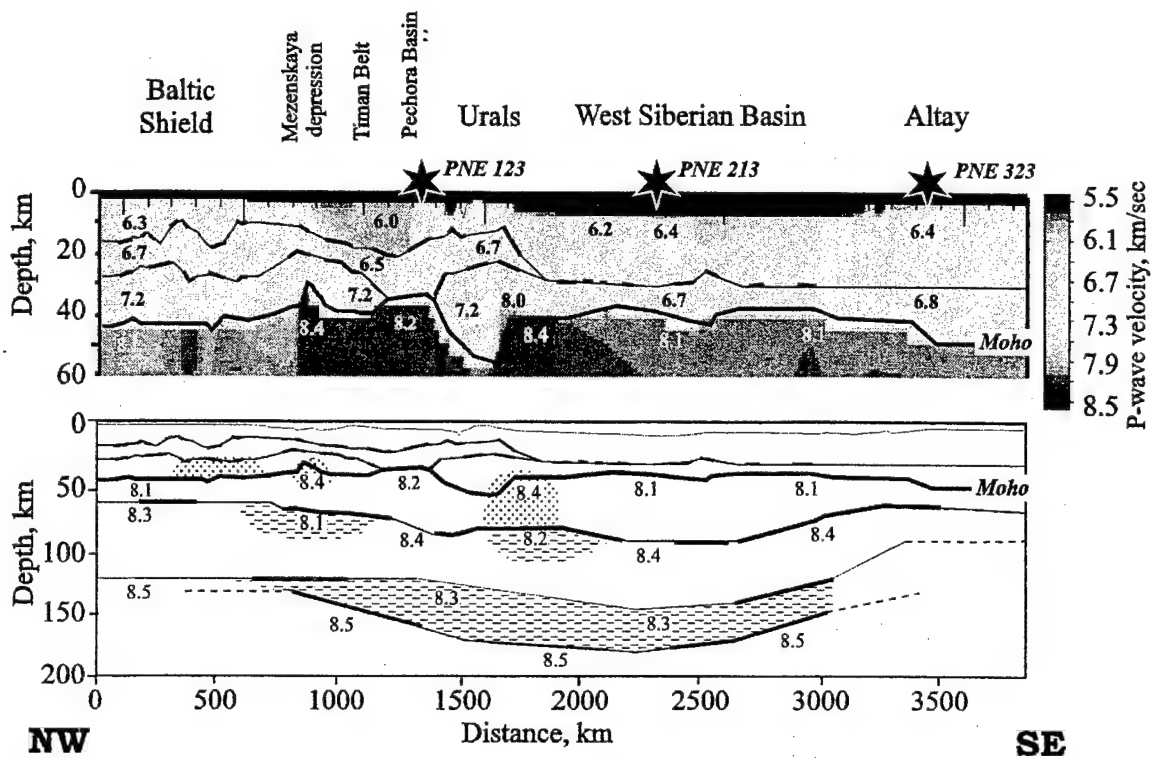
Figure 4. Crustal (top) and uppermost mantle (bottom) velocity-interface structure along the profile "Quartz" obtained using 3 PNEs and all 48 chemical explosions. Locations of the PNEs are indicated. Reflecting boundaries in the crust and mantle are highlighted. *P*-wave velocity values are given in labels. Note the low-velocity zones (dashed areas), high-velocity regions (dotted), horizontal velocity variations within the mantle, and prominent mantle reflectors at the depths of 60-90 and 120-140 km. Also note the Moho relief, especially the roots under the Ural Mountains and the Moho uplift under the Mezenskaya depression.

CHAPTER 3

On the nature of the teleseismic P_n phase observed on the ultra-long range profile "Quartz", Russia

by Igor B. Morozov[1], Elena A. Morozova[1], Scott B. Smithson[1], and Leonid N. Solodilov[2]

[1]*Department of Geology and Geophysics, University of Wyoming, PO Box 3006, Laramie, WY 82071-3006*
[2]*Centre for Regional Geophysical and Geoecological Research (GEON), Moscow, Russia*

corresponding author:
> **Igor B. Morozov**
> Department of Geology and Geophysics
> University of Wyoming
> PO Box 3006
> Laramie, WY 82071-3006
> phone (307) 766 3363
> fax (307) 766 6679
> e-mail morozov@uwyo.edu

ABSTRACT

The most prominent secondary phase observed in the records from the ultra-long profile "Quartz" crossing northern Eurasia is the high-frequency long-range (teleseismic) P_n. This phase, propagating with the group velocity of about 8.1-8.2 km/sec to over 3000 km distances, dominates the records within the frequency range above about 5 Hz. Within this teleseismic P_n, we distinguish onsets of several branches having higher apparent velocities between 8.5-8.6 km/sec. Using travel-time modeling techniques, we associate the teleseismic P_n with whispering gallery modes traveling within the top 160 km of the mantle. The long incoherent coda of this phase results from scattering and from reverberations of seismic waves within the crust. The contrast in frequency contents between the teleseismic P_n and deeper refracted and reflected phases is explained by the increase of inelastic attenuation within the prominent low-velocity zone below the depth of about 150 km.

INTRODUCTION

Russian Deep Seismic Sounding (DSS) program produced unparalleled until now seismic datasets suitable for a detailed study of the seismic structure of the upper mantle. A characteristic feature of this program was the use of large chemical and nuclear explosions (PNEs) recorded by densely spaced (10-15 km) 3-component short-period (1-2 Hz) portable recording systems deployed along linear profiles. Recording ranges of PNEs exceeded 3000 km, allowing observations of seismic phases diving down to 800 km into the mantle (Egorkin and Pavlenkova, 1981; Ryaboy, 1989; Kozlovsky, 1990). The data from one of the best profiles of this program, "Quartz" acquired during 1984-87 have been extensively studied by several groups, providing information about the mantle structure (Mechie et al., 1993; Ryberg et al., 1995; Ryberg et al., 1996) and about the structure of the crust (Egorkin and Mikhaltsev, 1990; Schueller et al., 1997) of the northern Eurasia (Figure 1).

PNE records from "Quartz" profile show a consistent sequence of primary P-wave refractions in the first arrivals observed to the maximum offset of 3145 km (Figure 2). Based on the analysis of the first arrivals, Mechie et al. (1993) derived 1-D velocity models for different PNEs, and Ryberg et al. (1996) proposed a 2-D model of the mantle velocity structure, using all three PNEs of the profile (Figure 1).
Due to high energy of the sources, PNE records are abundant in seismic phases as secondary arrivals (Figure 2). Reflections from the 410-km and 660-km discontinuities in the mantle and a number of crustal multiples are easily recognized (Figure 2). Reversed PNE records reveal horizontal variations in the structure of the mantle within the length of the profile (Ryberg et al., 1996; Morozova et al., manuscript in preparation). Our attention in this paper will be concentrated on the phase which is not obvious in unfiltered gathers, but becomes dominant after high-pass filtering of the records above approximately 5 Hz (Figures 3 and 4). This phase is also observed in the radial and transverse components and in the records from the third PNE of "Quartz" profile (see plots in Ryberg et al., 1995).

Such high-frequency long-range (often called teleseismic) P_n phases, and corresponding S_n phases propagating within the uppermost mantle to 2000-3000 km distances were observed by many authors (e.g., Molnar and Oliver, 1969; Heustis et al., 1973; Walker 1977). These phases efficiently propagate through continental shields and deep-ocean basins, but appear to be blocked by major suture zones (Molnar and Oliver, 1969). Although it is generally accepted that these phases are due to some sort of waveguide mechanism, no agreement about the details of this mechanism exists. Depending on the mantle structure beneath the Moho, several models of these high-frequency long-range phases have been proposed: whispering-gallery (WG) waves within the upper mantle (Stephens and Isacks, 1977; Menke and Richards, 1980), guided wave in a high-velocity layer above a low-velocity layer (Mantovani et al., 1977), or transmission through a low-velocity layer beneath the Moho (Sutton and Walker, 1972). Long incoherent codas of teleseismic P_n and S_n arrivals are explained by scattering of high-frequency waves

within the crust and upper mantle (Richards and Menke, 1983; Menke and Chen, 1984) together with reverberations in the water column (Sereno and Orcutt, 1985, 1987).

Ryberg et al. (1995), who first observed this band of incoherent high-frequency energy in "Quartz" records, proposed a model that relates this phase to a special propagation mechanism through a strongly scattering waveguide located immediately below the Moho. Using simulations with the *reflectivity* method (Fuchs and Müller, 1971), Tittgemeyer et al. (1996) demonstrated that a high-frequency phase with an apparent velocity of about 8.1 km/sec can propagate by means of multiple scattering through a 80-km thick stochastic sequence of thin layers below the Moho.

Although presenting a possible propagation mechanism, this "multiply scattering waveguide" by Ryberg et al. (1995) and Tittgemeyer et al. (1996) does not appear to be the likely solution, since it implies very strong horizontal continuity of the scatterers. Strongly scattering mantle above 120 km would have been clearly recognized in earthquake codas. From the observational standpoint, this model does not account for three important details of the kinematics of this high-frequency phase in "Quartz" records: 1) the increase in its apparent velocity within the offset range of 1000-1700 km; 2) the separation of its onset into at least three branches with apparent velocities of about 8.5 - 8.6 km/sec between the offsets of 1300 and 2400 km; and 3) the presence of a high-frequency and high-velocity event at the offsets exceeding 2700 km, and 7 - 10 sec before the main teleseismic P_n (Figure 4). Also, the scattering-waveguide model does not explain the relation of the teleseismic P_n to other low-frequency phases, and in particular, the coincidence of the onset of this phase with the "internal multiple" m indicated earlier by Mechie et al. (1993) within the offset range 1000 - 1700 km (Figure 2). Finally, the unfiltered records from PNE 123 show that the teleseismic P_n between the offsets of 900 to 1700 km is remarkably strong and coherent (Figure 3), and therefore it definitely cannot be due to a stochastic scattering mechanism.

As it often happens in seismology, another interpretation of these observations exists. In this paper, we re-examine the nature of the teleseismic P_n in "Quartz" records. After analyzing travel-time, amplitude, and spectral characteristics of a number of secondary phases, and after performing a simple simulation of scattering within the crust, we will arrive at a model of teleseismic P_n propagation that will be different from the stochastic model by Ryberg et al. (1995) and Tittgemeyer et al. (1996), but related to the more deterministic WG models proposed earlier (Menke and Richards, 1980). A cartoon shown in Figure 5 summarizes the main idea of our interpretation. Instead of speaking of the "high-frequency" teleseismic P_n, we recognize it as the first "broad-band" arrival at offsets exceeding 1000 km, in comparison to which the deeper refracted and reflected waves are relatively devoid of high-frequency energy. This observed penetration depth-dependent frequency selectivity is associated with the increase of seismic attenuation with depth.

TELESEISMIC P_n IN "QUARTZ" RECORDS

Analyzing the nature of the incoherent "high-frequency" teleseismic P_n phase in "Quartz" records, we need to explain three major observed characteristics of this phase:

1) its travel-time dependence and relations to other seismic phases;
2) clear separation in frequency content from the lower-frequency deep refractions;
3) its incoherence and the long incoherent coda.

Starting our analysis with the first of the above questions, and after travel-time forward modeling of the major phases contributing to the observed wavefield, we present a simple simulation of the kinematic effects of scattering in the first-order Born approximation. After this, we describe how the attenuation within the upper mantle can cause the observed frequency separation of the teleseismic P_n from deep mantle refractions. After that, we briefly discuss the possible role of scattering effects in the formation of the coda.

In the subsequent analysis, we will use the records of the southern "Quartz" PNE (shot point 323 in Figure 1) having the largest signal-to-noise ratio within the high-frequency part of recorded bandwidth (Figure 2).

Phase correlation

The critical difference of our interpretation from that by Ryberg et al. (1995) lies in a different identification of the seismic phases (Figure 6). In the high-frequency filtered gathers (Figure 4), we see that the teleseismic P_n increases its apparent velocity toward smaller offsets, between 1000-1500 km, where it is close to the Moho multiple from the depth of about 90 km (Figure 6). The continuation of this phase toward the ordinary P_n is clearly of a significantly lower amplitude, and it is not seen in Figure 4. Teleseismic P_n becomes visible in the records (Figure 4) only near the triplication point of the first WG wave, following the onset of the Moho multiple from the depth of 90 km (Figure 6). This observation also argues against the "scattering waveguide" origin of the teleseismic P_n, since such scattering would have resulted in a uniformly decreasing amplitude with offset. Between the offsets of 1500 and 2700 km, the onset of the teleseismic P_n is apparently discontinuous, with a cusp near 2300 km (Figure 4). This travel-time pattern most likely corresponds to two WG branches with apparent velocities near 8.6 km/sec (Figure 6).

Travel-time analysis

To examine the travel-time pattern of seismic phases found in the records, we employ 2-D ray tracing in a spherically-symmetric 1-D model. Although ray tracing does not account for wave interference effects and cannot correctly predict amplitude variations in the presence of sharp velocity contrasts and shadow zones, it is still an excellent tool providing an insight into mutual relations between different types of seismic waves.

Using ray tracing, hypotheses about the origins of certain phases can be formulated and easily tested for correct kinematics. Shooting at controlled angular intervals, we in many cases can approximately estimate relative amplitudes of the waves by comparing ray densities at receiver points or by calculating wavefront curvatures (Cerveny et al., 1984).

To explain the principal relations of the observed seismic phases, 1-D model developed using the first breaks picked from the records of the same southern PNE is quite appropriate (Mechie et al., 1993; Figure 7). The velocity column associated with this PNE is characterized by a strong velocity gradient between 90 and 120 km, a narrow low-velocity zone (LVZ) between 140 and 155 km, and a prominent LVZ with a moderate velocity gradient between 195 and 380 km depth. The 410-Km discontinuity is placed at 420 km in this model. This velocity structure explains the first breaks very well, including the 400-km long shadow zone between the offsets from 1500 to 1900 km (Figure 2; see also Mechie et al. 1993). The quality of the first arrivals from all three "Quartz" PNEs, and especially from the southern PNE, is high, and allows a confident identification of described velocity gradients within the upper mantle. Although certain difficulties are encountered in the integration of this velocity column with that corresponding to the northern PNE (Mechie et al., 1993; Ryberg et al., 1996), these difficulties do not affect our interpretation of the upper-mantle-guided seismic phases.

The results of our travel time modeling of the main phases propagating in this 1-D velocity structure that are summarized in Figure 8 and are compared to the high-frequency record section in Figure 9. As Figure 9 shows, the first WG mode corresponds to the observed teleseismic P_n throughout its entire observation length. The WG mode appears at offsets of about 400 - 500 km and has a significant amplitude in between the offsets of 1500 to 2000 km, representing the first strong arrival in this region. Toward smaller offsets, its travel-time curve can be continued as that of a multiple between a reflector at about 90 km depth and the Moho, as labeled in Figure 2. At larger offsets, this phase continues to the end of the offset range with an apparent group velocity of 8.2 km/sec (Figure 8). Note that the second WG mode appearing at the offsets of about 2200 km can be also identified in the records (compare Figure 4 to Figure 9). Due to the variations of the velocity gradient above 140 km depth (Figure 7), this WG mode exhibits a triplication near 1800-2000 km, with the fast branch having an apparent velocity of 8.7-8.8 km/sec (Figure 8). Both WG branches are barely visible in unfiltered records (Figure 2), but become discernible in the high-pass filtered records of Figure 9, after the low-frequency reverberations of the first arrivals have been attenuated.

Based on the above observations—on the high amplitude of the WG phase observed from 1500 to 2000 km of offset in unfiltered records, on the travel-time match of this phase with the teleseismic P_n throughout the entire offset range, and on the observation of the triplication of the teleseismic P_n at about 2000 km—we conclude that the WG mode presents a good explanation of the kinematics of the observed teleseismic P_n

phase. As we see in Figures 3 and 4, the travel-time curve of the long-range P_n *does not* approach that of the ordinary P_n with decreasing offsets, but follows the moveout of a multiple reflection from a depth of approximately 90 km. Therefore, the long-range P_n cannot originate immediately below the Moho, as it was suggested by Ryberg et al., (1995) and Tittgemeyer et al. (1996), but should effectively be produced by the velocity gradient between 90 and 120 km depth (Figure 7).

A significant feature of the high-frequency wavefield is the presence of energy propagating earlier and faster then the teleseismic P_n at offsets exceeding 2700 km (Figure 4; it is also labeled in Figure 9. Note, however, that recording systems of a different type were used at the offsets above 2700 km, and thus the records may look more discontinuous across the White Sea). The calculated fast travel-time branch WG_1 has a correct travel-time placement and moveout, but terminates at offsets of about 2700 km due to its plunging into the LVZ (Figure 8). This inconsistency of the model is apparently due to its simplified 1-D character and should be resolved in a future 2-D model that will include the information from refracted, reflected, and WG waves from all 3 PNEs. Most likely, the increased amplitude of the WG_1 mode at far offsets marks the termination and/or deepening of the asthenospheric LVZ toward the Baltic Shield.

High frequency of the long-range P_n: a constraint on the attenuation within the upper mantle

A simple "first-order" explanation of the differences in frequency contents of the seismic phases shown in Figures 2 and 4 is readily obtained from an examination of the penetration depth diagram shown in Figure 8. The near-offset high-frequency refracted mantle wave seen up to nearly 1500 km offset is significantly attenuated beyond the distance of 1000 km (Figures 2 and 4), which corresponds to the penetration depth of about 150 km (Figure 8). Likewise, the high-frequency WG modes observed between the offsets of 800 km and 2800 km do not dive deeper then about 150 km into the mantle. On the contrary, the deeper and faster branch WG_1 is significantly attenuated between 2000 - 2700 km of offset (Figure 9). In addition, Figure 8 shows that all far-offset and low-frequency refractions penetrate at least to the depth of 270 km. All these observations suggest that the low-velocity structures below the level of 150 km may cause attenuation sufficient to explain the observed amplitude decay of the deeper phases at the frequencies near and above 5 Hz. Since the total propagation times of the deep phases are *smaller* than those of the waveguide modes, a significant increase in the attenuation should occur below the depth of about 150 km.

Although the depth level at which the increase of the attenuation occurs is constrained by the above observations as close to 150 km, its accuracy is limited by the use of the 1-D velocity model (Figure 7) and by the ray-theoretical approximation employed. Therefore, we do not attempt to obtain a more precise estimate for the depth of the contrast, or to correlate our 1-D attenuation model with the detailed velocity column shown in Figure 7. Instead, we assume a simple two-layer attenuation structure, with the quality factors Q above the level of 150 km and Q_{LVZ} below it, and look for a relation $Q_{LVZ}(Q)$ between them.

To constrain the amount of the attenuation increase, we calculate the relative energy dissipation factor between two selected frequencies during the propagation of a deep refracted wave:

$$A_{12}^{deep} = 10 \cdot \lg\left(\frac{E(f_1)}{E(f_2)}\right) = 10 \cdot \lg e \cdot \left(\frac{2\pi}{Q}t_s + \frac{2\pi}{Q_{LVZ}}t_d\right)(f_2 - f_1). \qquad (1)$$

This equation describes the increase in the ratio of the low-frequency spectral density (frequency f_1) to the high-frequency spectral density (frequency f_2), in dB. In this equation, the times that the deep refracted wave travels above and below the depth of 150 km are denoted as t_s and t_d, respectively. Subtracting from the quantity defined in Equation (1) a similar ratio for WG arrival, we obtain an expression for the observed logarithmic relative contrast between the two spectral constituents of these phases:

$$A_{12}^{deep} - A_{12}^{waveguide} = 10 \cdot \lg e \cdot \left(\frac{2\pi}{Q}t_s + \frac{2\pi}{Q_{LVZ}}t_d - \frac{2\pi}{Q}t_{wg}\right)(f_2 - f_1),$$

(2)

where t_{wg} is the total travel time of WG mode, taken at the same offset.
Note that the relative spectral densities calculated for the same type of phase in Equation (1) are independent of the receiver coupling variations, of the geometrical spreading factors, and of the Moho reflection coefficients (for WG phase), but depend on the source amplitude spectrum. The second relative spectral ratio given in Equation (2) does not depend on the source spectrum, and therefore it is suitable for attenuation estimates.

The relative spectral ratios (2) for two frequency bands 1.0-1.5 Hz and 4-6 Hz measured in the records between the offsets of 2000 and 2500 km are presented in Figure 10. As Figure 10 shows, the power spectral density in the first arrivals is by 10-12 dB lower then that in the teleseismic P_n. By using this value as the estimate of the spectral contrast, by picking characteristic travel times for these offsets from the plots in Figure 8: $t_d \approx 200$ sec, $t_s + t_d \approx 250$ sec, and $t_g \approx 260$ sec, and by varying Q, we obtain from Equation (2) the relation for the quality factor $Q_{LVZ}(Q)$ below the 150-km level shown in Figure 11. Although this estimate does not constrain the attenuation in the uppermost mantle, it demonstrates that a significant increase in attenuation below the 150 km level is necessary to explain the observed difference in the high-frequency content between the more shallow and deep refractions and reflections (Figure 11). Assuming that the attenuation above the LVZ corresponds to $Q \approx 400\text{-}600$ (Anderson and Given, 1982), we obtain from Equation (2) values $Q_{LVZ} \approx 320\text{-}400$ for the quality factor below the 150-km level (Figure 11). Note that the contrast between the attenuation above and within the LVZ increases with increasing Q.
Although the presence of the attenuation contrast at the top of the LVZ is confidently established through the observed contrast in the frequency contents of the signals (Figure 10), its simple estimate presented above can be improved in two ways: 1) the constraint shown in Figure 11 most likely *underestimates* the attenuation contrast, since

we have assumed that the zone of high attenuation extends to the depth of 410-km discontinuity, whereas this zone can be actually thinner; and 2) not only the relation $Q_{LVZ}(Q)$, but also the values Q_{LVZ} and Q themselves can be measured from the records, yielding an independent way of obtaining a high-resolution image of the upper mantle attenuation structure. We will address these issues in a forthcoming paper.

The physical causes of the observed mantle attenuation might be scattering by mantle heterogeneities as well as inelastic energy dissipation. However, the clear onset of the high-frequency energy (Figure 4) suggests that the increase of attenuation below the level of 150 km occurs predominantly due to the increase in the intrinsic (inelastic) attenuation. Indeed, elastic scattering tends to delay the arrival of high-frequency energy, while intrinsic absorption removes it from the wavefield (Richards and Menke, 1983). The records show that the increase of the high-frequency energy is strongly correlated with the WG modes, and is not related to the scattering from the deeply refracted waves (Figure 9). Even if the scattering mantle heterogeneities were located above the depth of 150 km, as Ryberg et el. (1995) have suggested, they would produce some pattern of high-frequency scattered energy following the first arrivals which is not found in the records.

Multiples and scattering

The above travel-time simulations correctly indicate the position of the onset of the teleseismic P_n but do not account for the diffuse onset of this phase and for the presence of a long incoherent coda. These features can be explained by the scattering occurring within the crust and/or upper mantle.

To allow the propagation of high-frequency energy to substantial distances, the scattering within the uppermost mantle should be weak. An alternative proposed and modeled by Tittgemeyer et al. (1996) is a layered structure exhibiting strong multiple scattering in the vertical direction and almost no scattering horizontally. Although possible, this alternative does not seem to be likely, since it would imply a very high aspect ratio of the heterogeneities.

On the contrary, the crust represents a waveguide trapping postcritical P_g and S_g waves and propagating them to large distances. The Moho irregularities, surface and basement topography, and the variations in the crustal velocity along the profile (Schueller et al., 1997) provide the heterogeneities that should be sufficient to generate the teleseismic P_n coda. Assuming that the scattering is moderate, we can use a low-order Born approximations to estimate its influence on the pattern of the recorded wavefield. In our modeling, we analyze only the kinematics of the scattering by shooting pairs of rays from scattering points in random directions, and by constructing a scattering pattern for each phase shown in Figure 5. The scatterers' depths and scattering angles are uniformly distributed, and thus the modeled offset-traveltime pairs build up a pattern of probable scattering paths from point scatterers. To produce a more physically realistic

picture of scattering including scattering amplitudes, a more rigorous modeling using a 2-D mantle velocity/attenuation model is certainly required.

The results of ray tracing in the same 1-D velocity model (Figure 7) with random scattering heterogeneities located within the crust are shown in Figure 12. In our simulation, we included the first multiples from the free surface and from the Moho boundary (Figure 5). Figure 12 shows that even first-order scattering within the crust complemented by multiples might account for the about-20-sec long codas of the WG modes. This scattering also creates long trains of P_g energy lasting for about 40-50 sec in our simulation (note, however, that from the amplitude considerations the dominant contribution to the coda should come from P-to-S_g scattering). Since up to 3-4 crustal multiples are observed in PNE records (Figure 2), we expect that the real scattering pattern involving 3-4 scattering and free-surface/Moho/basement reflection events would be much more complicated and extended in time.

Coda

The high-pass filtered records show a long coda following the teleseismic P_n arrival (Figure 4) apparently different from the amplitude pattern in the unfiltered records (Figure 2). However, as **3** shows, this difference is not so significant. In **3**, we present averaged amplitude decay curves measured within the offset range of 2500 - 2600 km, using the standard RMS measure of the vertical component and a 3-component instantaneous vector measure (Morozov and Smithson, 1996). In both cases, the signal was filtered below or above 5 Hz and the amplitude was averaged within a 2-sec sliding time window. Similar to what has been observed by Kennett (1993), the vector measure provides significantly more stable amplitude estimates.

The amplitude decay plots in **3** show that the teleseismic P_n is represented by a peak similar in duration to the onset of the first arrivals, followed by a long (up to 200 sec) train of crustal reverberations. Note that the high-frequency component actually decays a little *faster* than the low-frequency component, which is consistent with higher attenuation and scattering losses for shorter wavelengths. For both low-frequency and high-frequency components of the coda, the amplitude decay rate is close to *time*$^{-\frac{1}{2}}$ (**3**), corresponding to the propagation of surface- or guided waves. As it was outlined in the previous section, by far the most likely waveguide for these waves is represented by the crust. P_n and WG waves approaching the crust at grazing angles of incidence are strongly coupled to the relief on the Moho, on the top of the basement, on the free surface, as well as to crustal heterogeneities, generating postcritical shear-wave energy which is favored for lateral propagation in the crust (Dainty and Schultz, 1995). Also, an examination of the low-frequency records in Figure 2 shows that the coda of the WG mode is structured, including a sequence of prominent Moho multiples and higher-order WG modes.

DISCUSSION

Our interpretation of the teleseismic P_n phase observed in the records from *Quartz* PNEs differs significantly from the interpretation of the same phase by Ryberg et al. (1995) and leads to a dramatically different (although more conventional) upper mantle model. Therefore, a discussion of the differences of these models is necessary. We will focus this discussion on several principal aspects of the interpretation.

Physics of wave propagation. The "scattering waveguide" proposed by Ryberg et al. (1995) still needs to prove its viability through a theoretical analysis or 2-/3-D finite-difference simulation. From a general wave propagation standpoint, scattering does not seem to be able to provide a sufficient mechanism to ensure a predominantly horizontal propagation of seismic energy. 1-D simulations by Tittgemeyer et al. (1996) used as an evidence for a "totally new" phase describe a *totally different* physical situation of a stack of infinite thin layers that of course *do* form a waveguide. On the contrary, the well-established velocity gradient and the presence of the strong Moho and free-surface reflectors ensure an efficient propagation of the low-order WG modes.

Travel-time characteristics. Our interpretation accounts for three observed features of the teleseismic P_n travel time character: 1) the increased moveout between the offsets of 1000-1500 km; 2) the presence of two branches corresponding to different orders of WG modes; and 3) the presence of high-frequency energy 7 - 10 sec before the main branch at the offsets exceeding 2700 km (Figure 4). These details were not considered by Ryberg et al (1995) and were not explained by the "scattering waveguide" theory.

Amplitude characteristics. Although a rigorous amplitude analysis of DSS data still presents a formidable problem, it can be seen that the observed amplitude pattern of the teleseismic P_n does not correspond to the model of a shallow "scattering waveguide". Indeed, since the waveguide propagates the energy horizontally from the near-shot region, the amplitude of the phase would be expected to decrease continuously with distance. In the records of Figure 4, however, we see that the teleseismic P_n appears essentially after the onset of the multiple $P_{M90}P$, which corresponds well to its interpretation as the WG mode.

The sharpness of the teleseismic P_n onsets. The main point of the argument by Ryberg et al. (1995) against the WG interpretation is the absence of sharp onsets of the teleseismic P_n in the high-pass filtered records. However, an examination of both unfiltered (Figure 2) and high-pass filtered records (Figure 4) shows that the teleseismic P_n is sharp where it approaches the first arrivals (between the offsets of 1000 and 1600 km). In the records from PNE 123, a coherent first WG phase is seen even before its triplication point (Figure 3). The teleseismic P_n becomes not coherent in the secondary arrivals, after its enhancement by heavy filtering (Figure 4). Such behavior can be explained as due to various reasons: 1) the PNE source signature is far from a minimum-delay signal, and therefore the signal remaining after the removal of most of its (low-frequency) energy may have no sharp onset; 2) scattering within the crust makes the onsets of high-frequency phases complicated by long codas and diffuse (Figure 12); 3)

the high-frequency teleseismic P_n interferes with the background of energy following the strong first arrivals, which also contributes to the variability of its onset; 4) the top of the basement, not considered in our simulations, also presents a strong reflector creating numerous multiples and P/S conversions that cannot be resolved at the scale of this experiment; 5) with trace spacings exceeding 10 km, the data are strongly spatially aliased at 5 Hz, and therefore we cannot expect to observe significant spatial coherency. Due to these reasons, we find that the fine-scale shapes of the onsets of the teleseismic P_n do not carry any evidence against our WG model, and also they do not require multiple scattering within the mantle for their explanation.

Coda. An over 20-sec long coda of the teleseismic P_n arrival forms the second basis of the argument by Ryberg et al. (1995) and Tittgemeyer et al. (1996) against its WG origin. However, their analysis showing that the coda cannot be built up of WG branches was based on 1-D simulations using the *reflectivity* technique. On the contrary, our measurement of the coda amplitude decay rate carried out above suggests that the coda can be satisfactorily explained by crustal-guided waves (L_g, R_g) propagating within the crust, in a manner similar to the explanations of regional P-wave codas (see, e.g., Dainty and Schultz, 1995).
Synthetic seismograms calculated using the *reflectivity* method (see Figure 7 in Mechie et al. (1993)) show strong first WG and clear first free-surface WG modes supporting our ray tracing analysis. Due to the limitations of the algorithm (truncation errors, numerical underflow, computation time), a robust computation of the amplitudes of the higher-order WG modes arriving between the offsets of 2000 and 3000 km still presents a difficulty. Also, these amplitudes should be sensitive to the horizontally heterogeneous structure of the upper mantle not accounted for in 1-D models employed by the *reflectivity* approach. Nevertheless, our conclusion about the increased attenuation within the LVZ will remain valid regardless of the amplitude modeling technique, since it is based on the basic observation obtained directly from the data—the seismic phases that arrive earlier are attenuated stronger.

CONCLUSIONS

Based on our analysis of the secondary phases observed in the records from the PNEs of the ultra-long DSS profile "Quartz", we propose an interpretation of a long-range (teleseismic) P_n phase as a whispering-gallery wave traveling within the uppermost mantle. This conclusion is supported by the 2-D travel-time forward modeling of all observed phases using a detailed 1-D velocity model derived earlier. The long incoherent coda of this phase is associated with the scattering and reverberations of seismic waves within the crust, including its basement and the sedimentary cover. To explain the difference in the frequency contents between the teleseismic P_n and other refracted and reflected phases recorded at offsets exceeding 2000 km, we infer an increase in attenuation within the prominent low-velocity structures beginning at the depth of about 150 km. No scattering within the uppermost mantle is required to

explain the observed characteristics of the wavefield, and absorption is the most likely mechanism of the attenuation increase.

REFERENCES

Anderson, D. L. and J. W. Given (1982). Absorption band Q model of the Earth, *J. Geophys. Res.*, **87**, 3893-3904.

Cerveny, V., L. Klimes, and I. Psencik (1984). Paraxial ray approximation in the computation of seismic wavefields in inhomogeneous media, *Geophys. J.*, **79**, 80-104.

Dainty, A. M. and C. A. Schultz (1995) Crustal reflections and the nature of regional P coda, *Bull. Seismol. Soc. Am.*, **85**, 851-858.

Egorkin, A. V. and A. V. Mikhaltsev, (1990). The Results of Seismic Investigations along Geotraverses, in K. Fuchs, Y. A. Kozlovsky, A. I. Krivtsov and M. D. Zoback (Editors), Super-Deep Continental Drilling and Deep Geophysical Sounding, Springer, Berlin, 111-119.

Egorkin, A. V., and N. I. Pavlenkova (1981). Studies of mantle structure in the U.S.S.R. territory on long-range seismic profiles, *Phys. Earth Planet Inter.*, **25**, 12-26.

Fuchs, K., and G. Müller (1971). Computation of synthetic seismograms with the reflectivity method and comparison with observations, *J. R. Astronom. Soc.*, **23**, 417-433.

Heustis, S., P. Molnar, and J. Oliver, (1973) Regional S_n velocities and shear velocity in the upper mantle, *Bull. Seismol. Soc. Am.*, **63**, 469-475.

Kennett, B. L. N. (1993). The distance dependence of regional phase discriminants, *Bull. Seismol. Soc. Am.*, **83**, 1155-1166.

Kozlovsky, Y. A. (1990). The USSR Integrated Program of Continental Crust Investigations and Studies of the Earth's Deep Structure under the Globus Project, in *Super-Deep Continental Drilling and Deep Geophysical Sounding*, Fuchs K., Kozlovsky Y. A., Krivtsov A. I. and Zoback M. D. (Editors), Springer, Berlin, 90-103.

Mantovani E., F. Schwab, H. Liao, and L. Knopoff (1977). Teleseismic S_n: A guided wave in the mantle, *Geophys. J. R. Astron. Soc.*, **51**, 709-726.

Mechie, J., A. V. Egorkin, K. Fuchs, T. Ryberg, L. Solodilov, and F. Wenzel (1993). P-wave velocity structure beneath northern Eurasia from long-range recordings along the profile Quartz, *Phys. Earth Planet* Inter., **79**, 269-286.

Menke, W. H., and P. G. Richards (1980). Crust-mantle whispering gallery phases: A deterministic model of teleseismic P_n wave propagation, *J. Geophys. Res.*, *85*, 5416-5422.

Molnar, P., and J. Oliver, Lateral variations of attenuation in the upper mantle and discontinuities in the lithosphere (1969). *J. Geophys. Res.*, **74**, 2648-2682.

Morozov, I. B., and S. B. Smithson (1996), Instantaneous polarization attributes and directional filtering, *Geophysics,* **61**, 872-881.

Richards, P. G., and W. Menke (1983). The apparent attenuation of a scattering medium, *Bull. Seismol. Soc. Am.*, **73**, 1005-1022.

Ryaboy, V. (1989). Upper mantle structure studies by explosion seismology in the USSR, Delphic Associates, 138 pp.

Ryberg, T., F. Wenzel, J. Mechie, A. Egorkin, K. Fuchs, and L. Solodilov (1996). Two-dimensional velocity structure beneath Northern Eurasia derived from the super long-range seismic profile Quartz, *Bull. Seismol. Soc. Am.,* **86**, 857-867.

Ryberg, T., K. Fuchs, A. V. Egorkin, and L. Solodilov (1995). Observations of high-frequency teleseismic P_n on the long-range Quartz profile across northern Eurasia, *J. Geophys. Res.,* **100**, 18151-18163.

Schueller, W., I. B. Morozov, and S. B. Smithson (1997). Crustal and uppermost mantle velocity structure of northern Eurasia along the profile Quartz, *Bull. Seismol. Soc. Am.,* **87**, 414-426.

Sereno, T. J., and J. A. Orcutt (1985). Synthesis of realistic oceanic P_n wave trains, *J. Geophys. Res.,* **90**, 12755-12776.

Sereno, T. J., and J. A. Orcutt (1987). Synthetic P_n and S_n phases and the frequency dependence of Q of oceanic lithosphere, *J. Geophys. Res.,* **92**, 3541-3566.

Stephens, C., and B. L. Isacks (1977). Toward an understanding of S_n: Normal modes of Love waves in an oceanic structure, *Bull. Seismol. Soc. Am.,* **67**, 69-78.

Sutton, G. H., and D. A. Walker (1972). Oceanic mantle phases recorded on seismograms in the northwestern Pacific at distances between 7° and 40°, *Bull. Seismol. Soc. Am.,* **62**, 631-655.

Tittgemeyer, M., F. Wenzel, K. Fuchs, and T. Ryberg (1996). Wave propagation in a multiple-scattering upper mantle—observations and modeling, *Geophys. J. Int.,* **127**, 492-502.

Walker, D. A. (1977). High-frequency P_n and S_n phases recorded in the western Pacific, *J. Geophys. Res.,* **82**, 3350-3360.
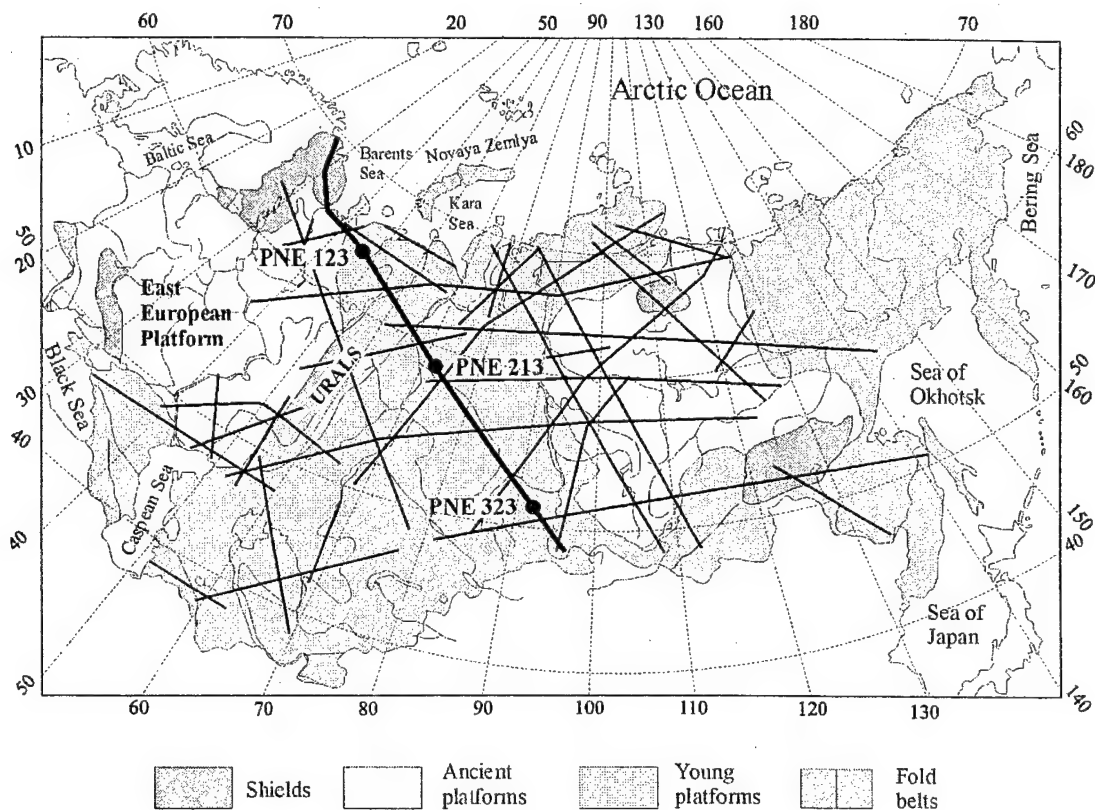
Figures

Figure 1. Map of the former USSR showing major DSS profiles using nuclear explosions. "Quartz" is shown in bold line; circles indicate the locations of three nuclear explosions recorded by the profile. The data from the southern and northern PNEs (shot points 323 and 123) are used in this paper.
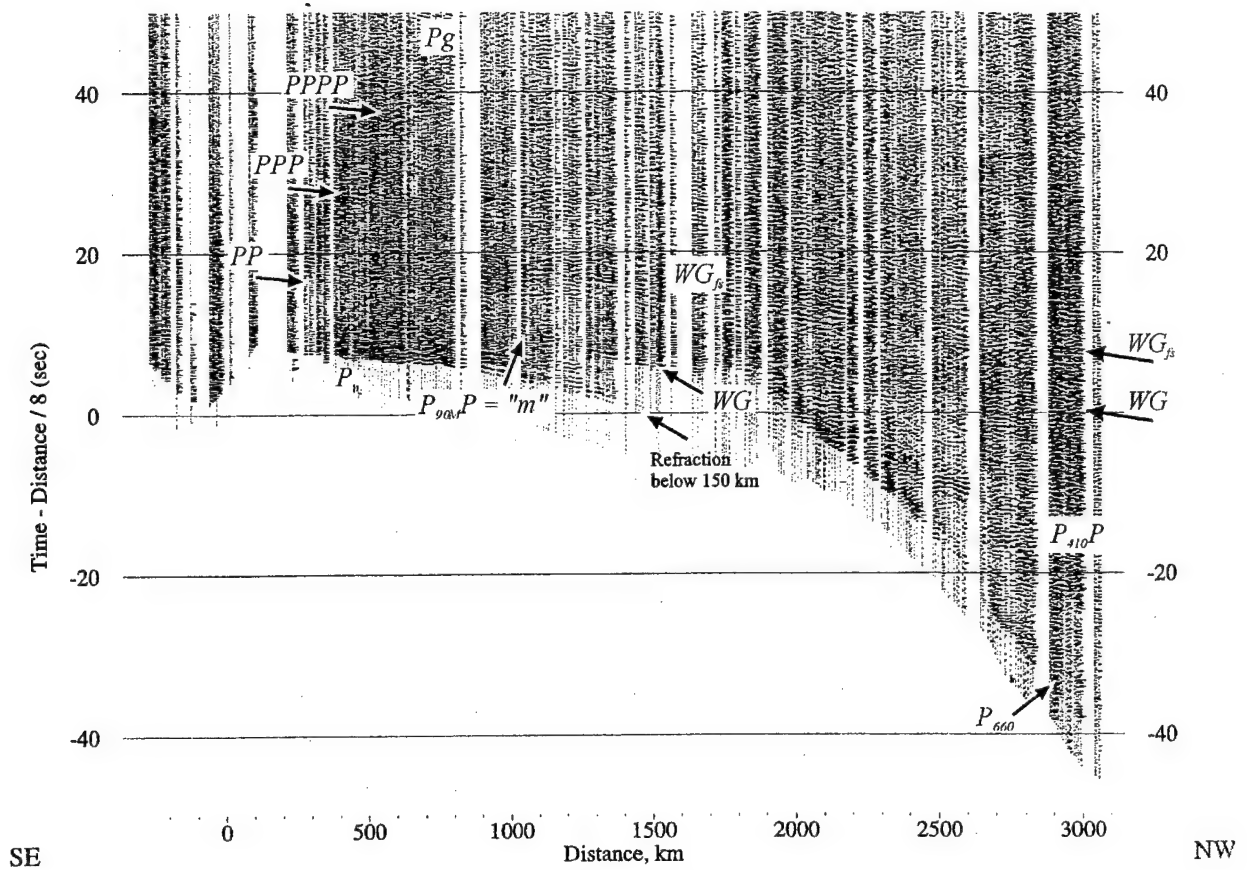
Figure 2. Vertical component record section from the southern PNE 323
of profile "Quartz". This PNE is characterized by the highest
amplitude of high-frequency signal. Reduction velocity is 8
km/sec. Primary refractions (P_n, P_{410}, P_{660}), P_g, reflection from
the 410-km discontinuity ($P_{410}P$), Moho multiple from 90 km
depth ($P_{90M}P$, labeled as "m" by Mechie et al. (1993)), and the
first whispering-gallery mode (WG) discussed in this paper are
indicated. WG mode is followed by a multiple, which we
associate with the free-surface WG mode (WG_{fs}). At offsets
below 1500 km, a series of Moho multiples can be seen (PP, PPP,
$PPPP$).
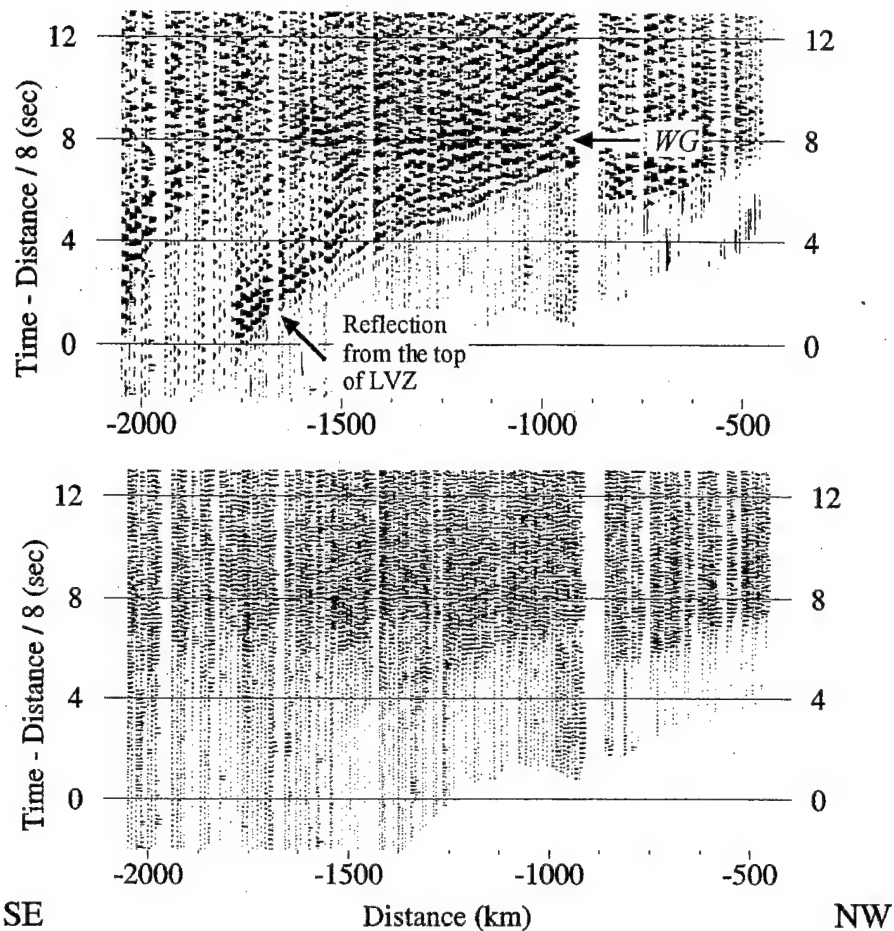
Figure 3. A segment of the vertical component record section from the
northern PNE 123 between the offsets 500 - 2000 km SE of the
source point (Figure 3). *Top*: unfiltered records; *bottom*: the same
records after high-pass filtering above 5 Hz. Reduction velocity is
8 km/sec. Note the strong and coherent whispering-gallery phase
(*WG*) propagating above the level of approximately 150 km and
dominating the high-frequency records. This phase is also strong
and coherent in the unfiltered records between the offsets of 900
and 1600 km. Also note the strong reflection from the top of the
asthenospheric LVZ beginning at about 200 km depth. This
reflection is practically absent from the high-frequency gather,
indicating the increase of attenuation between the depths of 150
and 200 km.
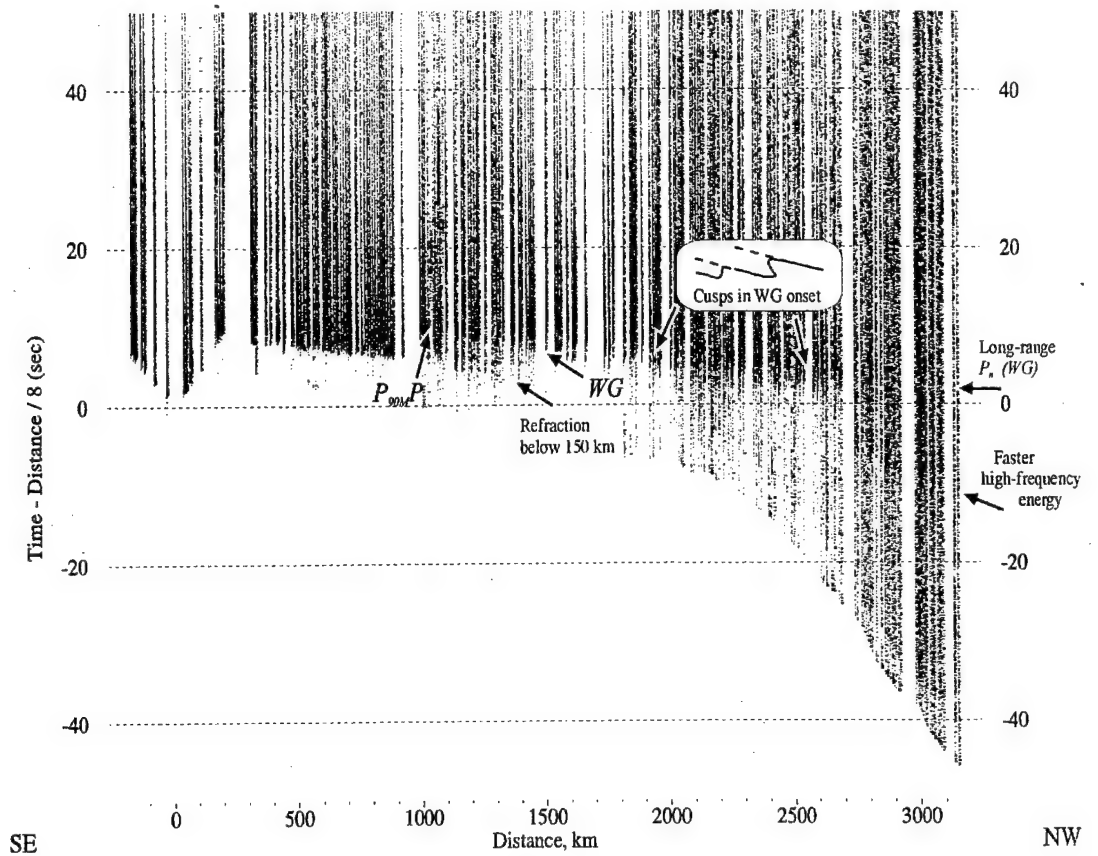
Figure 4. 3-component instantaneous vector amplitude gather of high-pass
filtered records from the southern PNE, obtained using the
technique described by Morozov and Smithson (1996). Vector
amplitude provides a more stable amplitude pattern facilitating the
identification of the WG modes. Reduction velocity is 8 km/sec,
corner frequency of the filter 5 Hz. This record is dominated by a
band of energy propagating with an apparent velocity of about 8.1
km/sec, corresponding to the teleseismic P_n phase. Despite an
incoherent nature of its onset, two branches (before and after 2300
km) can be distinguished. We associate this phase with two low-
order whispering-gallery (*WG*) modes. Note high-frequency
energy with faster apparent velocity arriving 7 - 10 sec earlier than
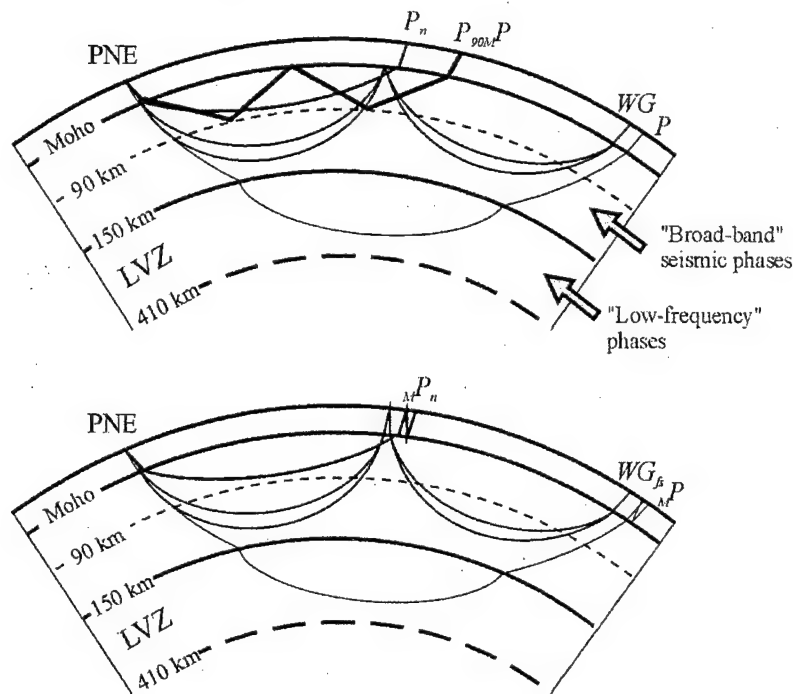this band at distances exceeding 2700 km.

Figure 5. A summary of our interpretation of observed high-frequency
phases in "Quartz" records. Drawn not to scale.

Top: P_n—refracted waves turning above the low-velocity zone (LVZ);
$P_{90M}P$— multiple reflection from the 90-km boundary and from
the Moho; WG—whispering-gallery modes (multiple refractions);
P—far-offset deep refraction arriving depleted of high frequency
energy. Triplication of WG modes due to the velocity contrast
within the 80 - 120 km depth range is indicated by double ray
paths. As we show, all "broad-band" phases (P_n, $P_{90M}P$, and
WG) do not penetrate into the LVZ, whereas the "low-frequency"
phases arriving beyond the offset of 1000 km travel within the
LVZ for over 150 sec.

Bottom: examples of major Moho multiples contributing to the coda
pattern: $_MP_n$—P_n multiple; $_MP$— multiple of the teleseismic
turning wave; WG_{fs}—free-surface WG mode. Other first-order
multiples of these phases (not shown for clearness) can be
constructed by including a ray bouncing within the crust into other
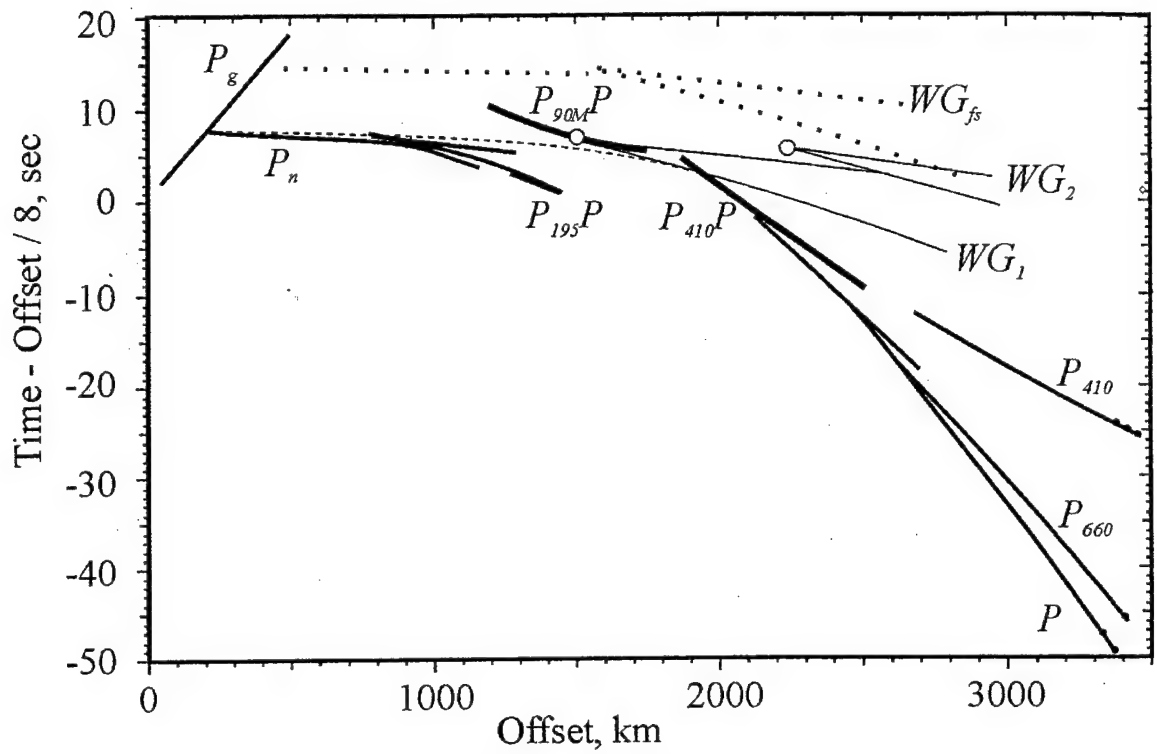branches of the corresponding rays.

Figure 6. A sketch of the travel time curves of the seismic phases
identified in Figures 2 and 4. Solid lines represent primary
refractions and WG modes. Dashed line shows the low-amplitude
near-offset part of the WG travel-time curve. Note the onsets of
different whispering-gallery modes WG_1 and WG_2 that we
associate with the observed undulations of the teleseismic P_n
onset between 1500 and 2700 km (Figure 4). Thick lines
represent the reflections from the top of the main LVZ ($P_{195}P$),
from the 410-km discontinuity ($P_{410}P$), and Moho multiple from
the depth of 90 km ($P_{90M}P$). Free-surface WG mode (dotted line,
WG_{fs}) contributes to the coda of the teleseismic P_n. Solid gray
circles indicate triplication points of the primary WG modes. See
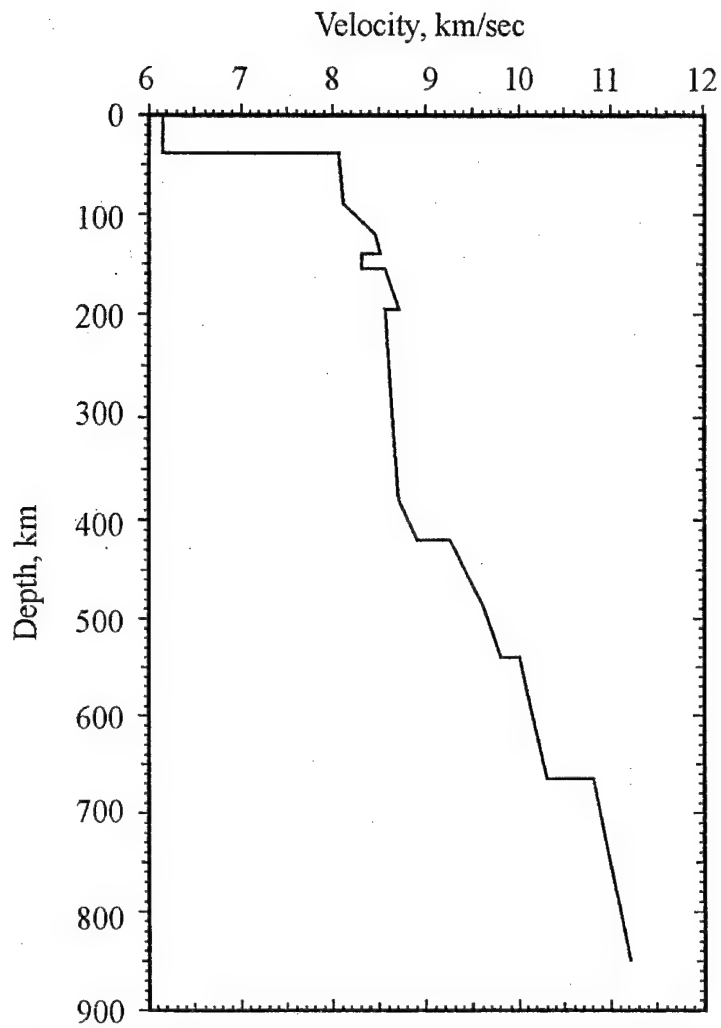discussion in the text.

Figure 7. 1-D velocity model obtained by Mechie et al. (1993) using first arrivals from the southern PNE. We used this model for 2-D ray tracing in our analysis of the kinematics of the teleseismic P_n. Note a LVZ between 140-155 km depth and a prominent LVZ below 195 km.
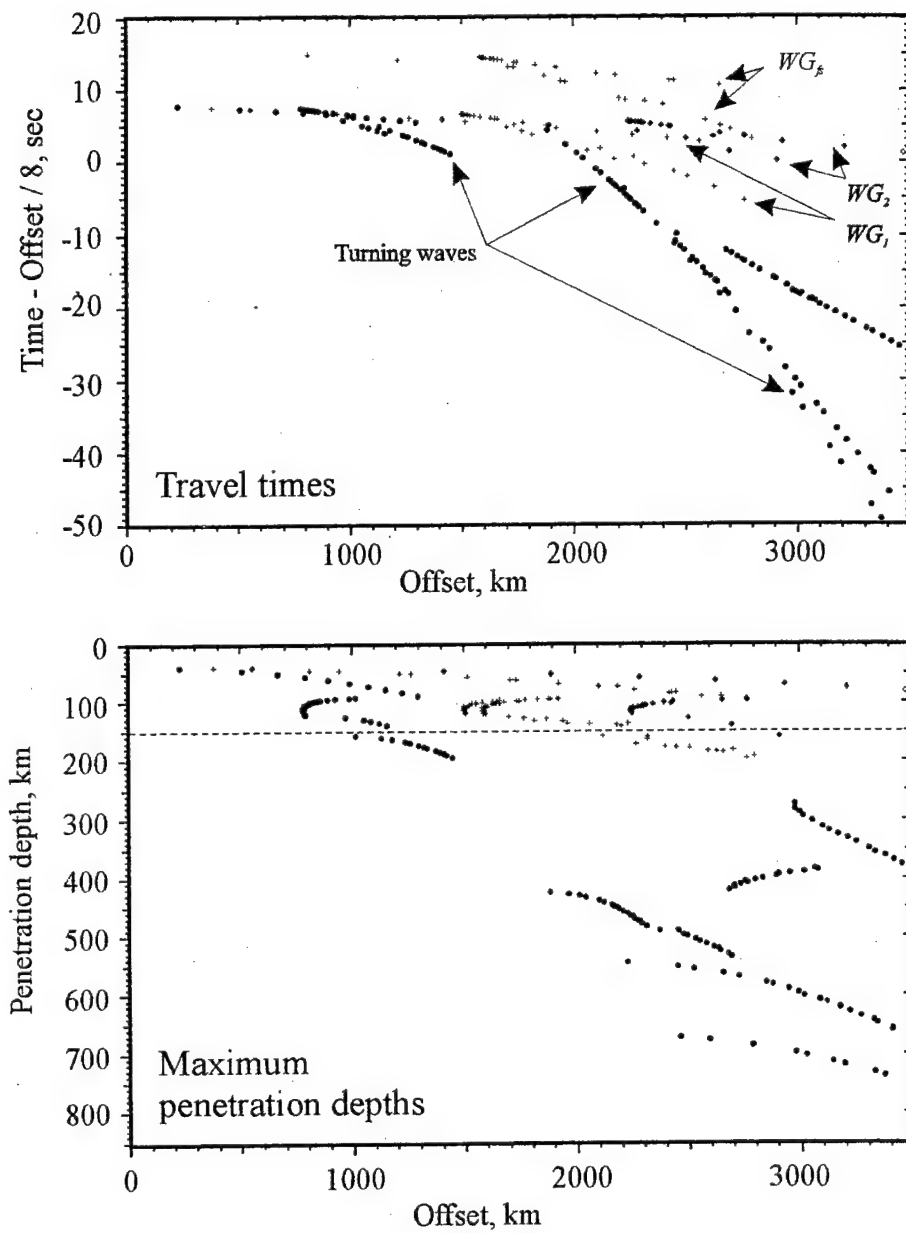
Figure 8. *Top:* travel time curves of the major phases. *Bottom*: maximum
penetration depths of refracted waves. Note that all "low-
frequency" waves arriving before WG modes penetrate into the
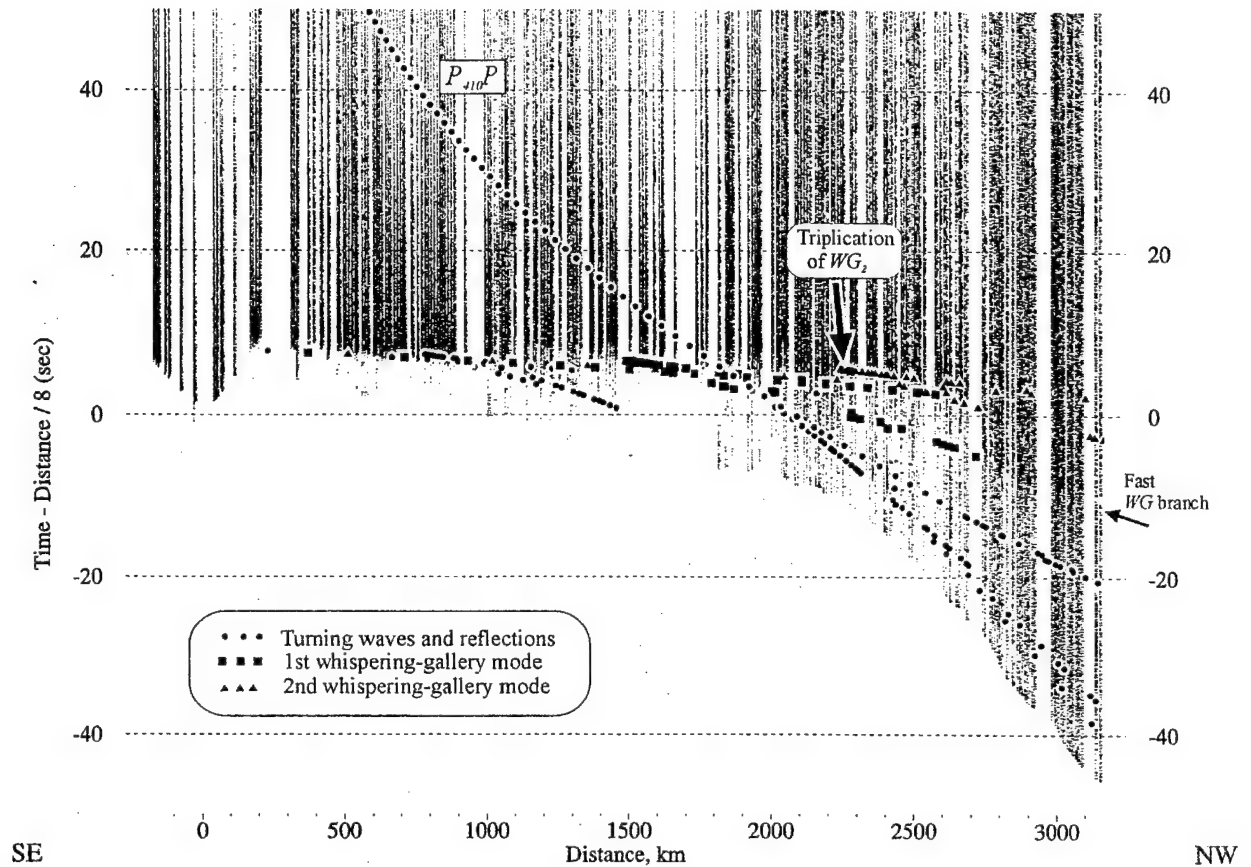two LVZs (Figure 7).

Figure 9. The same travel-time points as in Figure 8 overlain over the high-pass filtered record shown in Figure 4. WG modes correspond to the onset of the high-frequency teleseismic P_n. Note the triplication point of the second WG mode, also seen as a cusp in the onset of the teleseismic P_n in Figure 4. The fast branch of WG mode is observed, but can be followed to farther distances than in the modeled travel-time curves (indicated by an arrow on the right side of the section). Travel-time curve of the reflection from the 410-km discontinuity is also shown.
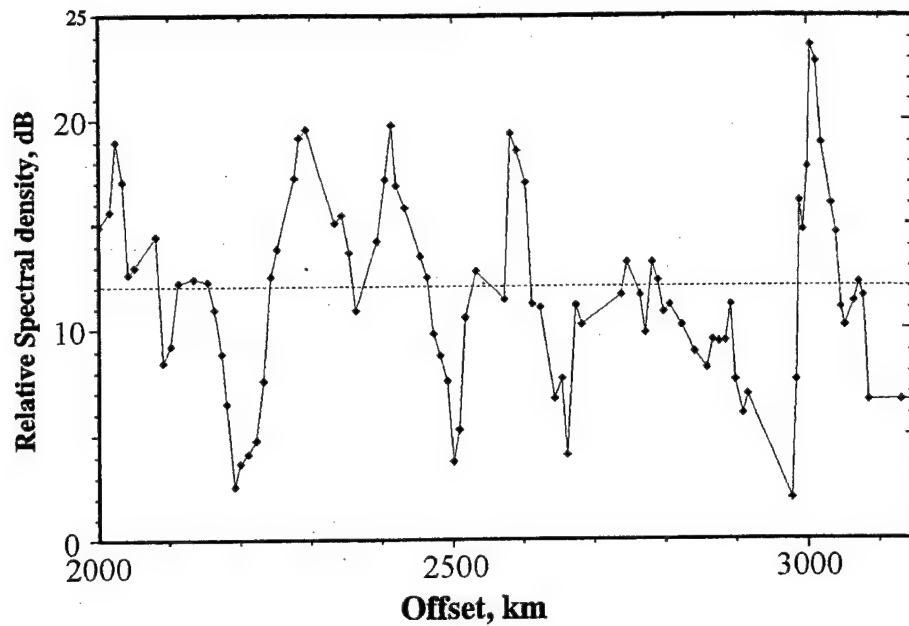
Figure 10. Spectral ratio of the teleseismic P_n to the first arrivals defined in Equation (2), measured for 1 - 3 Hz and 4 - 6 Hz frequency intervals within the offset range between 2200 - 3000 km. Note that the high-frequency content of the teleseismic P_n phase exceeds the corresponding level in the first arrivals by about 4 - 20 dB, with an average of 12 dB (dashed line).
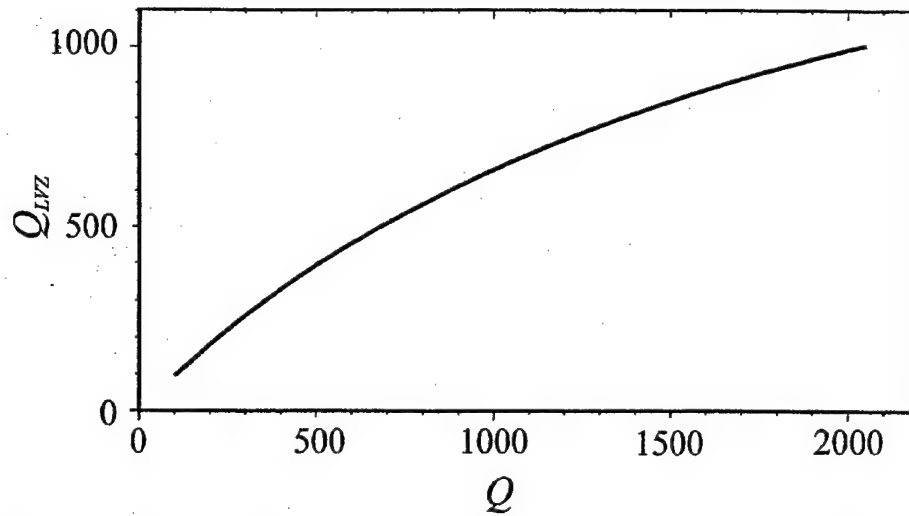
Figure 11. Constraint on the attenuation contrast at the top of the LVZ obtained from the ratios of power spectra of deep refractions and of the teleseismic P_n using Equation (2). Q and Q_{LVZ} denote the quality factor above and below the depth of 150 km, respectively.
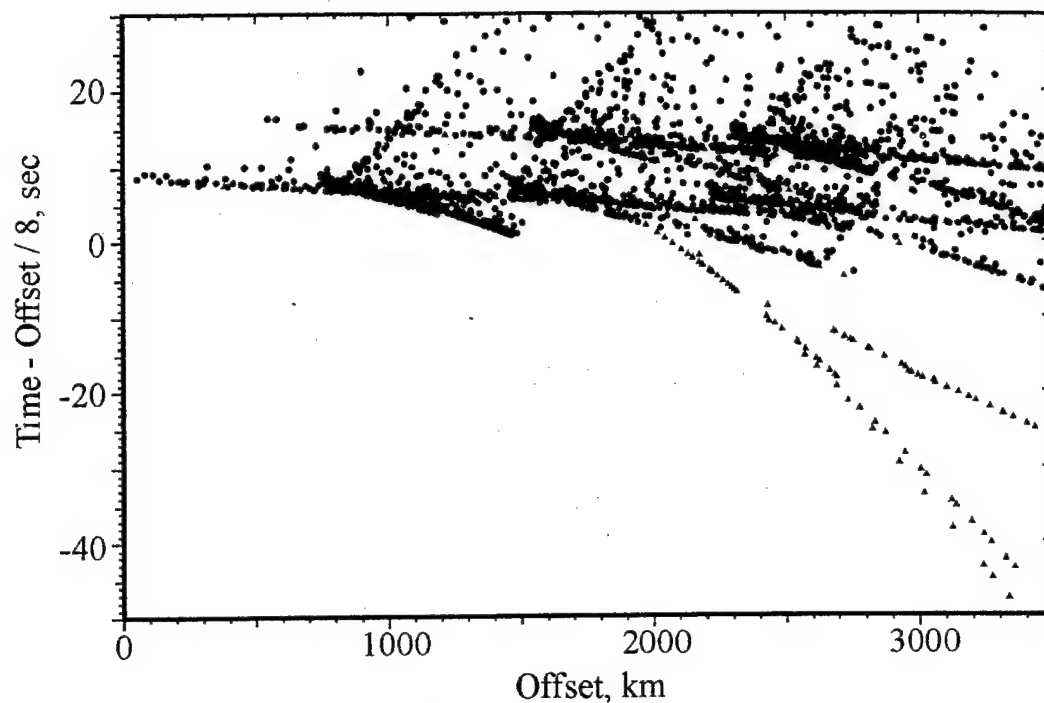
Figure 12. Travel-time plots obtained using ray tracing in the 1-D velocity
model shown in Figure 7 with first-order random scatterers
located within the crust. Note that already a single scattering
within the crust is kinematically sufficient to account for observed
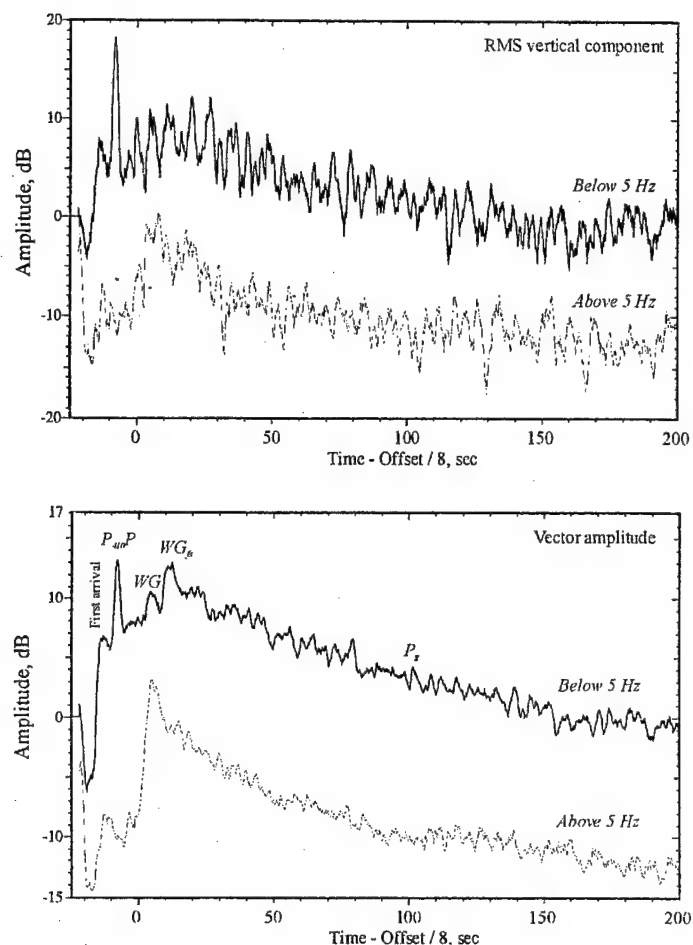codas of WG modes.

Figure 13. Amplitude decay curves of the high-frequency and low-frequency (filter corner frequency in both cases is 5 Hz) coda averaged within the offset range 2500 - 2600 km from PNE 323. *Top:* RMS amplitude of the vertical component; *bottom:* 3-component vector amplitude (Morozov and Smithson, 1996). In both cases, 8 km/sec time reduction was applied and the traces were stacked; after that, trace amplitude was calculated and averaged within a 2-sec sliding time window. Note that the vector measure provides considerably more stable amplitude measurements. First arrivals and two WG phases are indicated. Note that the high-frequency coda of WG mode is somewhat *shorte*r then the coda at low frequencies.

CHAPTER 4

Coda of long-range arrivals from nuclear explosions

Igor B. Morozov[1,2] and Scott B. Smithson[2]

[1]*Department of Geology and Geophysics, Rice University, MS-126, 6100 South Main Street, Houston, TX 77005-1892, USA*
[2]*Department of Geology and Geophysics, University of Wyoming, PO Box 3006, Laramie, WY 82071-3006, USA*

Corresponding author:

Igor B. Morozov

Department of Geology and Geophysics,
Rice University, MS-126,
6100 South Main Street,
Houston, TX 77005-1892, USA

Phone   (713) 285 5325
Fax   (713) 285 5214
e-mail   morozov@geophysics.rice.edu

Abstract

Short-period, three-component recordings from peaceful nuclear explosions (PNE) of the profile QUARTZ, Russia are used to constrain the nature of the coda of PNE arrivals. In particular, we examine the unusually strong and extensive coda of the long-range P_n (interpreted as a whispering-gallery, WG) phase propagating to beyond 3000 km. Energy-balance considerations in three dimensions show that such an extensive coda is inherent not only to WG but to all other P-wave phases and can be explained by crustal scattering. The long coda is a result of excitation of short-period scattered waves (P_g, S_g, L_g, R_g) within the crust by the waves incident from the mantle, or, conversely, by generation of mantle phases from crustal guided waves within the source region. The resulting estimates of coda Q range between Q=380 near 2 Hz and Q=430 near 5 Hz and can be associated with crustal attenuation including the sediments. Our coda model also explains quantitatively the observed build-up of the arrival amplitude with time and the apparent lack of a pronounced coda of the body-wave arrivals from the mantle transition zone. These effects result from adding up the energy of the later arrivals arriving during the codas of earlier arrivals. We "deconvolve" the overlapping coda patterns and show

that the true relative energies of the arrivals are significantly lower than the apparent energies measured from the raw records. A whispering-gallery interpretation of the long-range P_n and crustal scattering accounts for the entire range of observations of kinematic, spectral, and amplitude pattern of the PNE wavefield and allows the derivation of constraints on attenuation.

Introduction

Seismic studies, including deep refraction and reflection experiments using large chemical and nuclear explosions, have demonstrated strong heterogeneity of the uppermost mantle. Mantle heterogeneity is manifested in velocity contrasts and pronounced stratification of the lithosphere imaged by P/S wave conversions (e.g., Bostock, 1998), in mantle reflectivity (e.g., Pavlenkova, 1996; Morozova et al., 1999), and in variations of seismic attenuation (e.g., Der et al., 1986; Morozov et al., 1998a, 1998b). Mantle velocity gradients and reflecting boundaries form a relatively shallow (between 100 – 150 km depth) waveguide favoring propagation of seismic energy to teleseismic distances of up to 3000 km (Figure 2; Mechie et al., 1993; Ryberg et al., 1995; Morozov et al., 1998a). Such phases, known as long-range (teleseismic) P_n, were also identified in long-range profiles using large conventional explosions (Enderle et al., 1997; Henstock et al., 1998) and acquired critical significance for some interpretations of the fine-scale structure of the uppermost mantle (e.g., Enderle et al., 1997). Since these waves are confined within the uppermost 100 - 120 km of the mantle, amplitude and coda character carry important information about the structure of this region.

Two recent interpretations of the long-range P_n sharply diverge in their interpretations of the observations and in conclusions about the uppermost mantle structure. Based on one-dimensional (1-D) modeling of coda properties using the method by Fuchs and Müller (1971), Tittgemeyer et al. (1996), and Ryberg and Wenzel (1999) proposed a special, "high-frequency waveguide" propagation mechanism of the long-range P_n. These authors suggested a small-scale, random sub-Moho layering with high, 5% RMS velocity fluctuations and average layer thickness of 2 km within a zone extending 75 km below the Moho (Ryberg and Wenzel, 1999). Although faced with significant difficulties in petrologic interpretation of this model (e.g., Ryberg and Wenzel, 1999, p. 10,660), such strongly scattering uppermost mantle was viewed as a global phenomenon (Enderle et al., 1997).

In contrast to the above model, Morozov et al. (1998a) argued that the observations of the long-range P_n could be better explained by multiple sub-Moho refractions (whispering-gallery modes) within the uppermost mantle. According to this interpretation, no unusual wave propagation mechanism was required in order to explain the nature of this phase and no strong scattering within the uppermost mantle is required. At larger ranges, similar strong PP phases followed by extensive codas were identified in NORSAR recordings of nuclear explosions in Western Russia (Baumgardt, 1985). The enhanced high-frequency content of these phases relatively to the waves diving into the mantle transition zone was explained by increased attenuation below a depth of

about 150 km (Morozov *et al.*, 1998a, b). Morozov *et al.* (1998a) and Morozov (submitted) argued that the "scattering waveguide" model was primarily based on a misinterpretation of the apparently high-frequency character of the long-range P_n by Ryberg *et al.* (1995) and by the inadequate, 1-D models of its coda employed by Tittgemeyer *et al.* (1996) and Ryberg and Wenzel (1999).

Although kinematic behavior and spectral content of the long-range P_n does not present any difficulty for the whispering-gallery model (Morozov *et al.*, 1998a), the high amplitude of this phase and particularly its extensive coda (Figure 2) still need to be understood. Recent studies of the decay rate of this coda resulted in surprisingly high values of coda Q between 1000 - 2000 (Ryberg and Wenzel, 1999) or even 2000 - 5000 (Ryberg *et al.*, 1995). Such high Q values can hardly be associated with crustal attenuation, and as a result, extremely strong yet horizontally coherent scattering within the mantle was suggested (Ryberg *et al.*, 1995).

Although numerical modeling of three-dimensional (3-D) scattering effects of short-period PNE wavefields still presents insurmountable difficulties, scattering is still inherently a multi-dimensional process, and only accounting for 3-D wave propagation can explain the observed coda decay rate. Fortunately, the observed coda amplitude pattern allows an explanation from simple physical considerations of energy balance; such an explanation is the focus of the present study.

For our interpretation of the long-range P_n amplitude, we extract amplitude decay curves within 200 sec of a range of seismic records from PNE QUARTZ-4 (often referred to as PNE 323) where the separation of the phases provides the best illustration of the QUARTZ PNE energy pattern (Figures Figure 1 and 3, modified from Morozov *et al.*, 1998a). The energy in the PNE wavefield at this distance appears to build up for 20 – 30 s after the first arrivals, followed by an extensive coda that can be observed for 100 – 150 s (Figure 3). Both the high amplitudes of the WG phases and the coda are surprising and do not fit into conventional views. Specifically, we will seek answers to two intriguing problems of the recorded distribution of PNE energy (Figure 3):

1) What is the nature and decay character of the observed codas of PNE arrivals? Why is the coda of the free-surface multiple *PP* (*WG_{fs}* in our notation) much stronger than the coda of $P_{410}P$ reflections of nearly the same amplitude?
2) Why are the amplitudes of the WG phases so high compared to the reflections from the transition zone, whereas 1-D modeling shows much lower amplitudes (synthetic models were presented by Mechie *et al.* (1993) and Morozova *et al.*, (1999)).

These are precisely the questions put forward in support of the "scattering waveguide" interpretation by Ryberg and others; however, we emphasize that there is very little of a specific, "high-frequency" accent in these questions. Instead, these problems are more clearly posed by the low-frequency, high-amplitude pattern in Figure 3. Note that the

"scattering waveguide" model by Ryberg *et al.* (1995) is based solely on the high-frequency coda of *WG* whereas the low-frequency coda is stronger and longer, indicating that the scattering phenomenon is broadband and cannot be attributed to a tuned, high-frequency scattering within the uppermost mantle. Also, unlike the above authors, we consider the crust, as the most structurally and compositionally complex part of the Earth, also the most likely source of seismic scattering.

As we show below, a simple physical model of the coda allows us to obtain meaningful estimates of crustal attenuation quality factor (Q) and of the relative amplitudes of the arrivals without presently impractical 3-D finite-difference modeling. Our approach follows coda models accepted in teleseismic array observations (e.g., Greenfield, 1971; Bannister et al., 1990; Dainty, 1990; Gupta et al., 1991) and is based on two fundamental observations. Firstly, waves propagating through the mantle and incident on the crust at high apparent velocity form a source of scattered energy different from the point-source model commonly used in coda estimates. Thus a correct coda model must take into account the distributed character of its excitation. Secondly, despite their apparent difference, we postulate that *all* the mantle arrivals could have similar coda patterns. Due to their long extent, these codas overlap creating the stepwise increase in energy seen in Figure 3. Decomposition of the recorded amplitude pattern allows us to obtain the true relation between the amplitudes of the onsets of the different PNE phases and their codas.

Coda decay rate of the long-range PNE arrivals

Figure 3 shows that the two *WG* multiples forming the long-range P_n are clearly distinct in the character of their codas. The first, Moho multiple labeled *WG* in Figure 3 is followed by a coda that dominates the high-frequency record (Figure 2). However, in the low-frequency band, the strongest phase is the free-surface P_n multiple (WG_{fs}) followed by its coda. The higher amplitude of the WG_{fs} event is consistent with higher reflectivity of the free surface compared to the Moho. Also, the longer and low-frequency coda of WG_{fs} suggests a predominance of surface waves that propagate efficiently at lower frequencies and are progressively more attenuated as the frequency increases.

Previous measurements of coda decay rate by Ryberg *et al.* (1995) and Ryberg and Wenzel (1999) resulted in two conflicting estimates both of which suggested very high Q values over 1000 - 2000. However, values of Q might be overestimated from the use of a coda power decay rate (Aki and Chouet, 1975):

$$P(t) \propto t^{-\zeta} e^{-\omega t/Q},\qquad(1)$$

where t is the time after the arrival, ω is the frequency. In expression (1), the factor $t^{-\zeta}$ with $\zeta \geq 1$ describes the geometric spreading of the waves forming the coda, and the quality factor Q corresponds to the attenuation. Ryberg and Wenzel (1999) used a preset value of $\zeta = 2$ assuming body-wave nature of the coda waves and a point source.

However, as pointed out by Morozov *et al.* (1998a) and Morozov (submitted), the energy of the coda of the long-range PNE phases is better described by a relation (1) with $\zeta \approx 1.0$ for the higher-frequency coda and $\zeta \approx 0.9$ for the lower-frequency coda, with $Q=\infty$. This ambiguity in the determination of the attenuation factor Q using equation (1) illustrates the importance of a correct model of geometrical spreading. The tendency of the geometric spreading parameter ζ to values lower than 1 when $Q=\infty$ shows that formula (1) may not be applicable to the coda decay rate of the long-range PNE arrivals.

Assuming predominantly crustal origin of the coda waves, coda amplitudes of PNE arrivals in Figure 3 can be explained readily once we take into account that seismic waves propagating through the mantle and entering the crust form a source of scattered waves that is different from a point source implied by relation (1). High apparent velocity of the incident waves (8 – 10 km/s) exceeds the velocity of the crustal-guided waves (3.5 – 5.5 km/s) generated through conversions on the Moho, on the basement, on surface topography, and on other velocity heterogeneities. Note that the most efficiently propagating phases within the crust (in the frequency range 0.5 - 10 Hz), post-critically reflected S waves, or L_g (Campillo, 1987), tend to the lower limit of this velocity range. High velocity of the moving source of scattered waves leads to a distributed source of coda energy.

In order to derive a phenomenological model of PNE coda excitation, we assume for simplicity that the coda of a PNE arrival consists predominantly of L_g; however, the argument should hold for other types of waves trapped within the crust. A commonly used L_g amplitude decay relation (e.g., Campillo, 1987; McNamara et al., 1996) converted to power units is:

$$P(f, D) = \frac{1}{D^{2\gamma}} R(f) S(f) e^{-2\pi f D / v Q(f)}, \qquad (2)$$

where D is the hypocentral distance, R and S are receiver and source terms describing site effects at the recording and excitation points, respectively, f is the median frequency of the observed wave, v is the group velocity for L_g, γ is the exponent of the geometric spreading within the medium, and Q is the quality factor of L_g propagation within the crust. Since the duration of L_g increases with distance, γ is larger than the value of 0.5 used for regional surface waves (Frankel *et al.*, 1990), and a value of $\gamma=0.83$ is generally accepted for L_g amplitude measurements in the time domain (Campillo, 1987, 1990; McNamara, 1996).

The expression (2) gives L_g power at distance D from the excitation point. By multiplying this expression by a time windowing function ("wavelet power") $W(t-t_0, D)$ we transform it into a phenomenological time distribution of recorded L_g power at time t:

$$P(t, D) = \frac{W(t - t_0, D)}{D^{2\gamma}} RS e^{-2\pi f D / v Q}, \qquad (3)$$

where t is the recording time, t_0 is the L_g generation time (onset of the mantle arrival at the scatterer), and we have ignored the frequency dependence for simplicity. The function $W(t-t_0, D)$ describes the broadening of the L_g wavetrain of an original duration τ at larger distances, and can be approximated as:

$$W(t - t_0, D) = \begin{cases} 1 \text{ for } \dfrac{D}{v} < t - t_0 < \dfrac{D}{v} + \tau D^{2\gamma-1}, \\ 0 \text{ otherwise.} \end{cases} \qquad (4)$$

Relation (4) ensures energy balance in equation (3) without attenuation.

By integrating the recorded L_g power at recording point $\mathbf{r}$ and at time t over all source (scattering point) locations, we obtain an expression for the recorded coda power:

$$P(\mathbf{r},t) = R \int d^2\mathbf{r}_S \frac{W\left(t - \dfrac{|\mathbf{r}_S|}{v_a}, D\right)}{D^{2\gamma}} S(\mathbf{r}_S) e^{-2\pi f D / vQ}, \qquad (5)$$

where $\mathbf{r}_S$ is the surface integration point, v_a is the apparent velocity of the arrival generating the coda, $D = |\mathbf{r} - \mathbf{r}_S|$, and $S(\mathbf{r}_S)$ is the scattering power proportional to the incident wave power (Figure 4). Note that at a given time t, the recorded coda is built up of the waves scattered from within a ring *around* the recording point (Figure 4); the area of this ring increases with time due to its increasing radius and width.

In a simple approximation corresponding to our averaged measurement of coda decay (Figure 3), we assume in relation (5) $|\mathbf{r}_S|/v_a \ll D/v$, and $S(\mathbf{r}_S) \approx$ const, corresponding to a nearly simultaneous generation of scattered energy within the crust and on the Moho. The integration area in Figure 4 then becomes circular, and the geometric spreading and the time window factors cancel. Therefore, instead of relation (1), the coda of a PNE arrival is better described by a simple exponential expression (with $\omega=2\pi f$):

$$P(t) \propto \widetilde{P}(t) = e^{-\omega t / Q}. \qquad (6)$$

A similar equation for coda energy was also derived by Dainty (1985).

The logarithmic amplitude plot (Figure 5) shows that the dependence (6) fits the observed coda amplitudes throughout $100 - 150$ s of the coda. These linear trends of $\ln P(t)$ are consistent with log-RMS coda shapes of Semipalatinsk nuclear explosions presented by Baumgardt (1985). From these trends, we estimate the quality factor as $Q=320$ near 2 Hz and $Q=430$ around 5 Hz (Figure 5).

Although we did not attempt to carry out a rigorous study of frequency-dependent attenuation, the two values above suggest a dependence of $Q \approx 270 \cdot f^{0.3}$. This moderate increase of Q with frequency agrees with values obtained for stable tectonic areas, such as the central US (Nuttli, 1982), the Canadian Shield (Hasegawa, 1985), or central France (Campillo, 1987). The resulting coda Q estimates are consistent with the values characteristic for the crust and support our association of the coda with L_g (Singh and Herrmann, 1983; Dainty, 1990). The comparatively low values of $Q \approx 270$ at 1 Hz

might be related to the effect of the thick sedimentary cover of the Pechora basin sampled by the part of the profile used in this analysis (Morozova *et al.*, 1999). However, this suggestion needs to be verified by a more detailed analysis.

Decomposition of PNE energy

The second problem posed in the Introduction, that of apparently much stronger coda of WG_{fs} compared to that of $P_{410}P$ (Figure 3) is resolved by the observation that the whispering-gallery phases arrive on top of the extensive codas of the preceding arrivals, resulting in buildup of the recorded energy. Thus the observed, overlapping amplitude pattern in Figure 3 must be "deconvolved" in order to extract the actual onset and coda amplitudes of the separate arrivals.

For a simple estimate of the actual arrival amplitudes, we model each of the events as a superposition of a primary arrival and of its coda (Figure 6). We assume that coda power follows the time dependence (6) and is proportional to the total energy of the primary phase. This approximation leads to a two-parameter amplitude decay model for each of the four arrivals labeled in Figure 3:

$$P\left(t-t^0\right)=\begin{cases} 0, & t<t^0, \\ \lambda P^0 \tau \widetilde{P}\left(t-t^0\right), & t\geq t^0, \end{cases} \qquad (7)$$

where t^0 is the onset time, P^0 is the squared amplitude of the onset, τ is the estimated duration of the primary phase (so that $P^0\tau$ measures its total energy), and λ is the relative coda amplitude parameter. Since we assume that the mechanism of scattering is common for all arrivals, λ is the same for P, $P_{410}P$, WG, and WG_{fs}. Thus the cumulative coda power at time t after the onset of WG_{fs} is:

$$P_{coda}(t) = P_P\left(t-t_P^0\right)+ P_{P410P}\left(t-t_{P410P}^0\right)+ P_{WG}\left(t-t_{WG}^0\right)+ P_{WGfs}\left(t-t_{FGfs}^0\right)+ P_{instr}\,.$$
(8)

In expression (8), we include an additive term P_{instr} describing the noise level of the instrument and of the recording site. We estimated this term from measurements of signal amplitude between $300-350$ s after the onset of the long-range P_n (the coda practically dissipates after about 150 - 200 s – see Figure 3).

Figure 3 shows that the $P_{410}P$ onset is sharper than those of the two WG modes. This comparative sharpness is expected since the WG modes enter the crust at larger angles, undergo additional reflections from the free surface and from the Moho, propagate within (most likely) a more complex lithospheric structure and thus should be more subject to perturbations. In our amplitude modeling, we reflect this sharpness by setting the duration of the P and $P_{410}P$ onsets equal to half of the duration of the WG and WG_{fs} modes. Note that the values τ and λ enter relations (7) only through their product, and thus the accurate absolute values of τ are not critical for coda modeling. We set $\tau=2.5$ for the two WG modes and $\tau=1.25$ for P and $P_{410}P$ phases.

By varying the remaining parameters corresponding to the four amplitudes and λ in relations (7) and (8) in order to match the observed amplitude variations, we obtained in the amplitude units of Figure 3: $A_P \approx 1.7$, $A_{P410P} \approx 4.1$, $A_{WG} \approx 2.1$, $A_{WGfs} \approx 2.9$, $\lambda \approx 0.22$. During this inversion, we also found that a value of $Q=380$ better describes the observed pattern of overlapping codas than the value of $Q=320$ estimated from the cumulative linear trend in Figure 5.

Figure 7 shows that the simple model (7)-(8) describes the observed amplitude pattern satisfactorily throughout the entire recording time range. As expected, the strongest phase in the "deconvolved" amplitude pattern in the bottom of Figure 7 is the reflection from the 410-km discontinuity. Note that because of increased attenuation below about 150-km depth (Morozov et al., 1998a, b), the arrivals from the mantle transition zone are very weak in the high-pass filtered records and they do not boost the apparent WG energy (Figure 3). Therefore, the high-frequency coda of the WG arrival in Figure 3 can be directly compared to our modeled WG coda in Figure 7. As expected, the low-frequency component of the WG phase is still stronger than the high-frequency part, reflecting the source spectrum dominated by the energy between 1- 2.5 Hz (Morozov et al., 1998b).

Energy pattern of PNE wavefield

As the argument above shows, the energies of secondary phases including the long-range P_n appear stronger than they are in reality due to their enhancement by the codas of the earlier phases. This observation helps us answer the second question posed in the Introduction. However, even after our amplitude correction, the amplitudes of the WG modes, and in particular, their total energy (Figure 7, bottom) are still significantly higher than expected from 1-D modeling (Mechie et al., 1993; Morozova et al., 1999). At longer ranges, high amplitudes of the surface multiples of P_n in this region are also indicated by the observations of a very strong PP phase (corresponding to the first phase in the WG_{fs} group in our notation) from the Semipalatinsk nuclear explosions (Baumgardt, 1985, 1990).

As a solution to this controversy, we consider two possible factors that could cause the increased energy of the WG modes and that cannot be accounted for in 1-D simulations. First, for a PNE near 700-m depth (Sultanov et al., 1999) the P-wave energy radiated at about 2-Hz frequency range (the dominant frequency of QUARTZ explosions; cf. Ryberg et al., 1995; Morozov et al., 1998b) is enhanced due to constructive interference with the pP reflection from the free surface (Fuchs, 1966; Greenfield, 1971). This interference would focus the energy in a downward direction increasing this energy by a factor of 10 – 13 compared to a source in an infinite medium (note that such interference might account for the 2-Hz peak frequency of the recorded energy). However, a point source is an oversimplified representation for a real explosion, and any irregularity of the source region or nonlinear effects would reduce such focusing (Greenfield, 1971). As a result, 1-D modeling tends to overestimate the downgoing energy at the expense of the modes propagating subhorizontally. For an explosion detonated within a

heterogeneous crust, we expect that a larger portion of energy would propagate in the form of the lithospheric-guided waves than predicted in 1-D simulations.

Another explanation for high amplitudes of the waves guided within the lithosphere could be their focusing under the northern part of the East European Platform. This region has a mantle structure that is distinctly different from that of the West Siberian basin (Mechie et al., 1997; Morozova et al., 1999 and personal communication). The unusually high amplitudes of the long-range P_n have been observed only on the profiles QUARTZ and RUBIN traversing the East European platform (Ryberg et al., 1995), and the strong PP phase was also identified practically along the path of the profile RUBIN (Baumgardt, 1985). On the contrary, our preliminary study (the Siberian PNE profiles have not been analyzed in full) suggests that the long-range P_n is much weaker and crustal attenuation is somewhat lower under the Siberian craton (Figure 8).

Although the above argument is only qualitative, note that not only the WG arrivals but also their primary phases P_n, and P_N (the latter are refractions and reflections from regional seismic boundaries between 90 – 140 km depth; cf. Pavlenkova, 1996; Morozova *et al.*, 1999) are very strong between the offsets of about 300 – 800 km (Figure 2). Such strong amplitudes should be due to high energy of the source and to the velocity gradient and reflectivity observed within the lithosphere (Morozova *et al.*, 1999). After a reflection from the Moho and free surface, this near-critical energy could form the observed strong waveguide arrivals (Figure 3).

Discussion

Since our coda decay model in equation (6) is dictated simply by the scattering geometry and by the principle of conservation of energy, it should be applicable to other observations of scattering at teleseismic distances. Indeed, in a teleseismic study of underground nuclear explosions at Novaya Zemlya, Greenfield (1971) interpreted the observed coda as a result of near-source $R_g \rightarrow P$ scattering and pointed out that without crustal attenuation, the coda energy would have been constant. Dainty (1990) suggested that for Kazakh nuclear tests recorded at NORESS, about half of the coda energy consisted of near-source $L_g \rightarrow P$ scattering, and another half was represented by $P \rightarrow L_g$ scattering near the seismic array, with an energy decay law similar to derived above (Dainty, 1985). Baumgardt (1985, 1990) used incoherent beams and continuous "polar scans" to identify variations in coda decay and mode content within 200 – 400 sec of the teleseismic P-wave codas.

Although the density of PNE recordings (10 - 15 km spacing) does not allow application of array methods for a detailed identification of the constituents of the coda (e.g., Bannister et al., 1990; Hedlin et al., 1994), the length of recording and the extent of coverage (Figure 2) allow measurements of the coda decay rate. Our model (Figure 7) shows that crustal-guided waves explain not only its amplitude decay but also the apparent lack of a pronounced coda of the body-wave arrivals from the mantle transition zone. Due to the slow coda amplitude decay rate, the codas of the PNE arrivals can be

observed to 100 – 150 s, and therefore the codas of multiple P-wave arrivals overlap and boost the energy of the later arrivals including the long-range P_n.

The coda of the WG phases and, as we suggested above, of all the other P-wave phases are not due to anomalously low crustal attenuation and to a tuned, narrow-band, highly scattering uppermost mantle as suggested by Ryberg *et al.* (1995) or by Ryberg et al. (1999). The coda is neither unusually high-frequency nor long to require such an interpretation. On the contrary, we favor the traditional interpretation of the coda as a result of crustal scattering of the waves incident from the mantle and propagating at high apparent velocities. The reciprocity principle complements this mechanism by its counterpart in which strong crustal-guided waves (P_g, S_g, L_g, R_g) generated by the PNE are scattered on crustal heterogeneities producing secondary phases propagating through the mantle and feeding the observed coda (Dainty, 1985, 1990).

Although our "instantaneous distributed coda source" model (6) above is only an approximation to the actual spreading coda source region, it is clearly more adequate than the point-source scheme (1) used by Ryberg *et al.* (1995) and Ryberg and Wenzel (1999). The relative velocities of the fast primary (P_n) to the slow scattered (L_g, R_g) phases lead to a distributed scattering mechanism and to the cancellation of the geometric factor in our coda decay relation (6). On the contrary, although the model by Ryberg *et al.* (1995) and Ryberg and Wenzel (1999) also implied distributed scattering (in their case, located within the mantle) these authors made no attempt to derive a proper coda relation for this scattering geometry. Instead, they resorted to a model of coincident coda source and receiver (Aki and Chouet, 1975) that is totally irrelevant in this case.

While attributing all scattering to the crust and Moho boundary, our argument does not eliminate the possibility of mantle scattering. Some degree of scattering should certainly be present in the uppermost mantle, yet such scattering is not required by the observations of PNE coda. At the same time, mantle scattering cannot be as high as suggested in the model by Ryberg and Wenzel (1999) in which the 75-km thick sub-Moho mantle reflects about 8-10 times more seismic energy than the Moho (as estimated by Morozov, submitted). Such strong scattering would most certainly destroy any coherent seismic waves penetrating through the uppermost mantle.

The above estimates of arrival amplitudes suggest that the dominance of the WG modes in the energy pattern of the PNE wavefield is to a certain degree apparent. Despite the high values of the observed amplitudes within the long-range P_n time window (Figure 3), both of the WG modes actually carry only about 75% of the power delivered to the surface by the $P_{410}P$ reflection. Since the $P_{410}P$ reflection is more coherent and shorter in duration, its coda is somewhat lower in amplitude yet it carries about 65% of the energy of both WG codas and about the same as the WG_{fs} coda alone.

Being significantly lower than it appears, the energy of the *WG* modes is still high compared to the predictions of 1-D simulations. As we suggested above, 1-D modeling of a PNE as a point source in a homogeneous crust could underestimate the amount of energy propagating in seismic phases guided within the crust and lithosphere. However, considering the uniqueness of the observation of high-energy long-range P_n under the East European platform and the West Siberian Basin, our preferred explanation of such high amplitudes is their being caused by focusing in these regions.

The high amplitudes of multiple refractions (*PP* and *WG*) could be qualitatively explained by the effects of crustal, Moho, and lithospheric heterogeneity favoring propagation of energy within the top 150 – 200 km of the mantle under the northern part of the East European platform and under the West Siberian basin (Figure Figure 1). Among these effects are the strong velocity gradient and reflecting boundaries in the uppermost mantle (Morozova *et al.*, 1999). As demonstrated by Kennett (1987), within the ranges of PNE profiles (20° to 30°) layered structures within the mantle may act as a wave guide contributing significantly to the *P*-wave coda.

Baumgardt (1985) also suggested that focusing could explain the high-amplitude *PP* in NORSAR recordings of the Semipalatinsk nuclear explosions. In particular, near-receiver focusing was required to account for the variations of *PP* amplitude across the array. In contrast to this observation, QUARTZ records show consistent and strong WG phases within the entire offset range and suggest that reflective lithosphere with vertical velocity gradient and favorable source conditions should be responsible for the overall character of the wavefield. Near-receiver scattering manifests itself in reduced coherency between the adjacent seismograms.

The unusually strong P_n and WG phases observed in QUARTZ records could support the observations of coda flattening between 310 – 450 sec after the teleseismic *P*-wave arrival in the recordings of Semipalatinsk explosions at NORSAR (Baumgardt, 1985, 1990). In a detailed study, Baumgardt (1990) showed that this part of the coda consisted primarily of L_g and S_n modes, with minor amounts of P_n energy and no detectable teleseismic *P* contribution. He interpreted this coda flattening as a result of $P_n \rightarrow L_g$ scattering under the Urals. This explanation, which appears to be the only reasonable model of the observed coda, also implies that the P_n is strong and carries enough energy to reverse the decay of the *P*-wave coda.

The observed difference between the amplitude dependencies of the records at lower and higher frequencies (Figure 5) is very significant. Similarly to the deep *P*-wave phases, the WG_{fs} arrival and its coda are low in their high-frequency content (Figure 5). Compared to *WG*, WG_{fs} is similar but travels two additional passes through the crust, and thus the disappearance of WG_{fs} in the high-pass filtered record should be related to crustal attenuation. Also, the increased Q at higher frequencies (Figure 5) and its regional variations (Figure 8) suggests that the low-frequency coda contains more

surface waves sampling the sedimentary, lower-Q parts of the upper crust. Therefore, the difference between WG and WG_{fs} also points to a crustal nature of the coda.

An important implication of our coda model is that only a three-dimensional (3-D) analysis of scattering can yield reasonable quantitative estimates of the dynamic properties of the PNE wavefield. Although 3-D or 2-D modeling of PNE short-period records using realistic crustal and mantle models is at present not practical, it appears that interpretations of scattering based exclusively on 1-D simulations (Tittgemeyer, 1996; Ryberg and Wenzel, 1999) might be misleading. On the contrary, energy balance considerations consistent with the accepted teleseismic coda models and utilizing the true, 3-D view of the process of wave propagation allow us to explain the behavior of the coda and to unravel the amplitude relations between the observed PNE phases.

Conclusions

The work presented above focused on the observed properties of the long-range PNE phases, and particularly, on the strong amplitude and long duration of the coda of the long-range P_n. Reconsidering the available observations of this phase in the records from the PNE profile QUARTZ, we arrived at both a consistent explanation of the character of this coda as well as at a realistic estimate of its decay rate, in contrast to some of the previous results (Ryberg et al., 1995; Tittgemeyer et al., 1996; Ryberg and Wenzel, 1999). The key points of our coda model of PNE arrivals are:

1) Regardless of the accepted explanation for the nature of the long-range P_n, a long coda is not specific to this phase but it follows every PNE arrival at an offset range over 2000 km;

2) The $100 - 150$-s long codas of the long-range arrivals are due to the generation of these codas within the crust by PNE phases propagating at high apparent velocities thus leading to distributed coda excitation and reduced geometric spreading;

3) The codas of the PNE arrivals build up energy within the record section leading to an increased energy within the long-range P_n time window; the amplitude pattern of the records was inverted for true amplitude relations between the arrivals.

Based on a detailed analysis of the long-range P_n, we demonstrated that this phase consists of two groups of arrivals that are clearly distinct in their frequency, amplitude, coda, and travel-time patterns. On the weight of such combined evidence, these arrivals are explained as the Moho and free-surface multiples of the refractions and reflections within the uppermost-mantle (P_n, P_N).

As a result of our PNE coda model, we obtained estimates of coda Q ranging between $Q=380$ near 2 Hz and $Q=430$ around 5 Hz. These values correspond to the values generally associated with the crust (including the sedimentary rocks) and suggest that the crust could be the source of the extensive coda pattern observed in PNE records (Figure 2). As our study shows, the amplitude pattern of the PNE records throughout

their full length can be explained quantitatively by body- and guided waves within the upper mantle and by (predominantly) crustal scattering.

References

Aki, K. and B. Chouet (1975). Origin of coda waves: source, attenuation, and scattering effects, *J. Geophys. Res.*, **80**, 3,322-3,342.

Bannister, S. G., E. S. Husebye, and B. O. Ruud (1990). Teleseismic *P* coda analyzed by three-component and array techniques: deterministic location of topographic *P*-to-*Rg* scattering near the NORESS array, *BSSA*, **80**, 1969-1986.

Baumgardt, D. R. (1985). Comparative analysis of teleseismic *P* coda and *Lg* waves from underground nuclear explosions in Russia, *Bull. Seism. Soc., Am.*, **75**, 1413-1433.

Baumgardt, D. R. (1990). Investigation of teleseismic *Lg* blockage and scattering using regional arrays, *Bull. Seism. Soc., Am.*, **80**, 2261-2281.

Bostock, M.G. (1998). Mantle stratigraphy and evolution of the Slave province, *J. Geophys. Res.*, **103**, 21,183-21,200.

Campillo, M. (1987). *Lg* wave propagation in a laterally varying crust and the distribution of the apparent quality factor in central France, *J. Geophys. Res.*, **92**, 12604-12614.

Campillo, M. (1990). Propagation and attenuation characteristics of the crustal phase *Lg*, *PAGEOPH,* **132**, 1-17.

Dainty, A. M. (1985). Air Force Geophysical Laboratory Report, AFGL-TF-86-0218.

Dainty, A. M. (1990). Studies of coda using array and three-component processing, *PAGEOPH*, **132**, 221-244.

Der, Z. A., A. C. Lees, and V. F. Cormier (1986). Frequency dependence of Q in the mantle underlying the shield region of Eurasia, Part III: The Q-model, *Geophys. J. R. Astr. Soc.*, **87**, 1103-1112.

Enderle, U., M. Titgemeyer, M. Itzin, C. Prodehl, and K. Fuchs (1997). Scales of structure in the lithosphere - Images of processes, *Tectonophysics,* **275**, 165-198.

Frankel, A., A. McGarr, J. Bicknell, J. Mori, L. Seeber, and E. Cranswick (1990). Attenuation of high-frequency shear waves in the crust: measurements from New York state, South Africa, and southern California, *J. Geophys. Res.*, **95**, 17441-17457.

Greenfield, R. J. (1971). Short-period P-wave generation by Rayleigh-wave scattering at Novaya Zemlya, *JGR*, **76**, 7988-8002.

Gupta, I.N., T. W. McElfresh, and R. A. Wagner (1991). Near-source scattering of Rayleigh to P in teleseismic arrivals from Pahute Mesa (NTS shots, in: Taylor, S. R., H. J. Patton, and P. G. Richards (Eds.), Explosion Source Phenomenology, *AGU Geophys. Monograph*, **65**, 151 - 160.

Hasegawa, H. S. (1985). Attenuation of L_g waves in the Canadian Shield, *Bull. Seism. Soc. Am.*, **75**, 1569-1582.

Hedlin, M. A. H., J.-B. Minster, and J. A. Orcutt (1994). Resolution of prominent crustal scatterers near the NORESS small-aperture array, *Geophys. J. Int.*, **119**, 101-115.

Henstock, T. J., A. Levander, C. M. Snelson, K. G. Miller, S. H. Harder, A. R. Gorman, R. M. Clowes, M. J. A. Burianyk, E. G. Humphreys (1998). Probing the Archean and Proterozoic lithosphere of western North America, *GSA Today*, **8**, 1-5.

Kennett, B. L. N. (1987). Observational and theoretical constraints on crustal and upper mantle heterogeneity, *Phys. Earth Planet. Interiors*, **47**, 319-332.

McNamara, D. E., T. J. Owens, and W. R. Walter (1996). Propagation characteristics of Lg across the Tibetian Plateau, *Bull. Seism. Soc. Am.*, **86**, 457-469.

Mechie, J., A. V. Egorkin, K. Fuchs, T. Ryberg, L. Solodilov, and F. Wenzel (1993). P-wave velocity structure beneath northern Eurasia from long-range recordings along the profile Quartz, *Phys. Earth Planet Inter.*, **79**, 269-286.

Mechie, J., A. V. Egorkin, L. Solodilov, K. Fuchs, F. Lorenz, and F. Wenzel (1997). Major features of the mantle velocity structure beneath northern Eurasia from long-range seismic recordings of peaceful nuclear explosions, *in:* Fuchs, K. (Ed.) Upper mantle heterogeneities from active and passive seismology, pp. 33-50, Kluwer Academic Publ., Dordrecht.

Morozov, I. B. Comment on "High-frequency wave propagation in the uppermost mantle" by T. Ryberg and F. Wenzel, submitted to *J. Geophys. Res.*

Morozov, I. B., and S. B. Smithson (1996). Instantaneous polarization attributes and directional filtering, *Geophysics,* **61**, 872-881.

Morozov, I. B., E. A. Morozova, and S. B. Smithson (1998a). On the nature of the teleseismic *Pn* phase observed in the recordings from the ultra-long profile "Quartz", Russia, *Bull. Seism. Soc. Am.*, **88**, 62-73.

Morozov, I. B., E. A. Morozova, S. B. Smithson, and L. N. Solodilov (1998b). 2-D image of seismic attenuation beneath the Deep Seismic Sounding profile "Quartz", Russia, *Pure and Applied Geoph.*, **153**, 311-348.

Morozova, E. A., I. B. Morozov, S. B. Smithson., and L. N. Solodilov (1999). Heterogeneity of the uppermost mantle beneath Russian Eurasia from the ultra-long range profile QUARTZ, *J. Geophys. Res.*, **104** (B9), 20,329-20,348.

Nuttli, O. W. (1982). The earthquake problem in the eastern United States, *J. Struct. Div. Am. Soc. Civ. Eng.*, **108**, 1302-1312.

Pavlenkova, N. I. (1996). General features of the uppermost mantle stratification from long-range seismic profiles, *Tectonophysics,* **264**, 261-278.

Ryberg, T., and F. Wenzel (1999). High-frequency wave propagation in the uppermost mantle, *J. Geophys. Res.*, **104**, 10,655-10,666.

Ryberg, T., K. Fuchs, A. V. Egorkin, and L. Solodilov (1995). Observations of high-frequency teleseismic P_n on the long-range Quartz profile across northern Eurasia, *J. Geophys. Res.,* **100**, 18151-18163.

Singh, S., and R. B. Herrmann (1983). Regionalization of crustal coda Q in the Continental United States, *J. Geophys. Res.,* **88**, 527-538.

Sultanov, D. D., J. R. Murphy, and Kh. D. Rubinstein (1999). A seismic source summary for Soviet Peaceful Nuclear Explosions, *Bull. Seism. Soc. Am.,* **89**, 640-647.

Thybo H. and E. Perchuc (1997). The seismic 8° Discontinuity and Partial Melting in Continental Mantle, *Science,* **275**, 1626-1629.

Tittgemeyer, M., F. Wenzel, K. Fuchs, and T. Ryberg (1996). Wave propagation in a multiple-scattering upper mantle—observations and modeling, *Geophys. J. Int.,* **127**, 492-502.

Ryberg T., M. Tittgemeyer, and F. Wenzel (1999). Propagation of elastic waves in the uppermost mantle, *Suppl to EOS, Trans., Am. Geophys. Union,* **80** (46), AGU Fall Meeting, San Francisco, CA, F712.
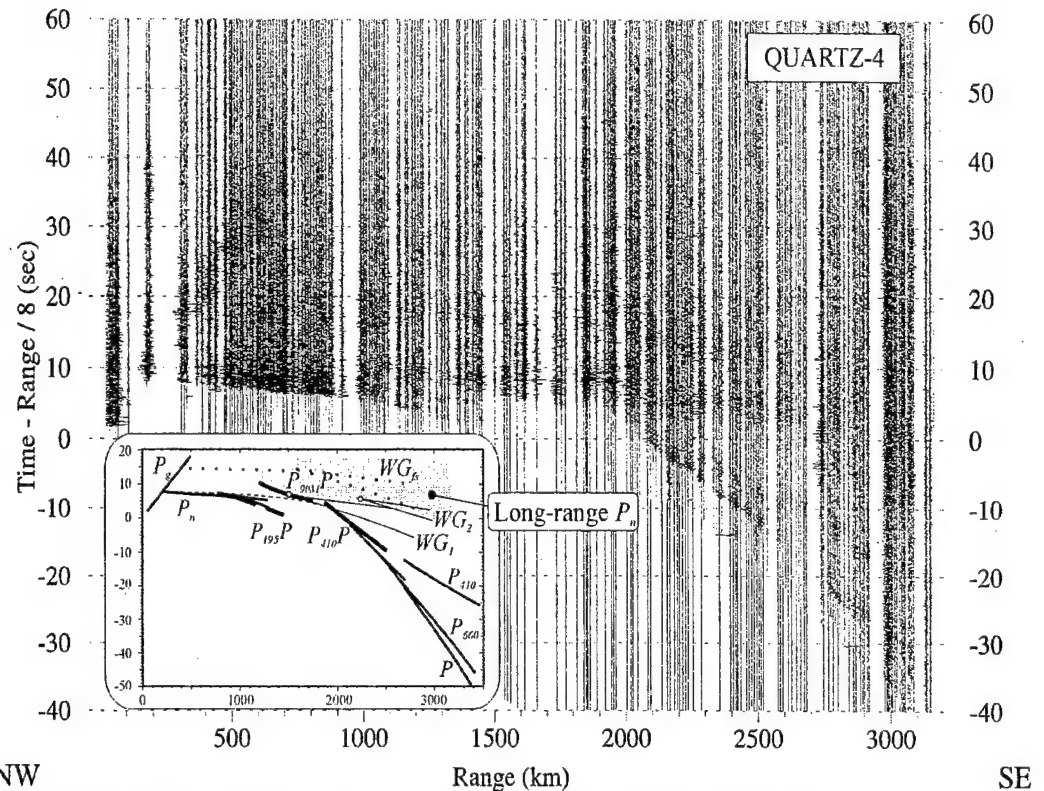
Figures
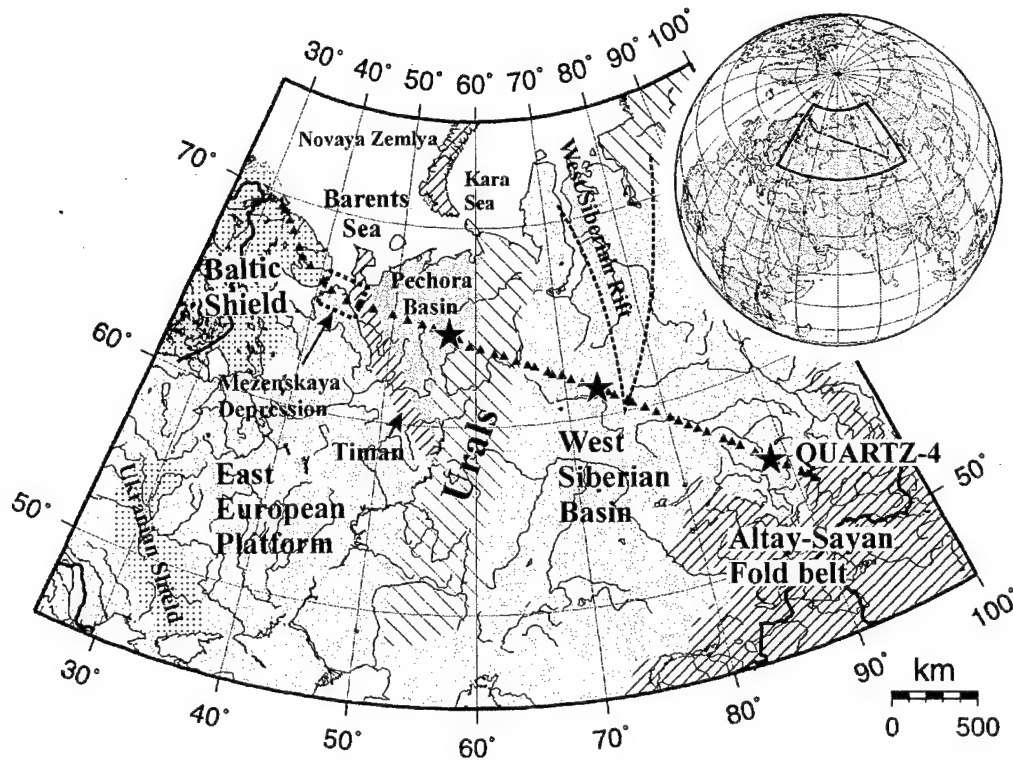
Figure 1. Map of the western part of the former USSR showing the profile QUARTZ. Triangles and stars indicate the locations of the chemical and nuclear explosions (PNEs) recorded by the profile, respectively, and PNE QUARTZ-4 is labeled. Major tectonic structures crossed by the profile are indicated. Dotted box near the Mezenskaya depression indicates the location of the receivers used in coda decay measurements in this study.

Figure 2. Vertical-component record from PNE QUARTZ-4 (Figure Figure 1; this explosion is also often referred as PNE 323). Inset shows a sketch of refracted, reflected arrivals and their multiples identified in this complex wave pattern. The long-range P_n phase (shaded in the inset) consists of a variety of arrivals forming a strong band of energy propagating to 3000 km at a group velocity between 8.0 – 8.1 km/s, with a faster branch at 8.5 km/s beyond 2700 km (Morozov et al., 1998a). Frequency content of this phase is close to that of the ordinary P_n (Morozov et al., 1998a), and after a high-pass filtering removing the deeper mantle body waves, this phase dominates the record (Ryberg et al., 1995). Note the unusually high energy of the arrivals in the primary P_n branch supporting the interpretation of the long-range P_n as a series of Moho and free-surface multiples of P_n and P_N (WG and WG_{fs}). Also note that the long-range P_n phase is strong and is followed by a coda extending beyond the ends of records shown here (Figure 3).
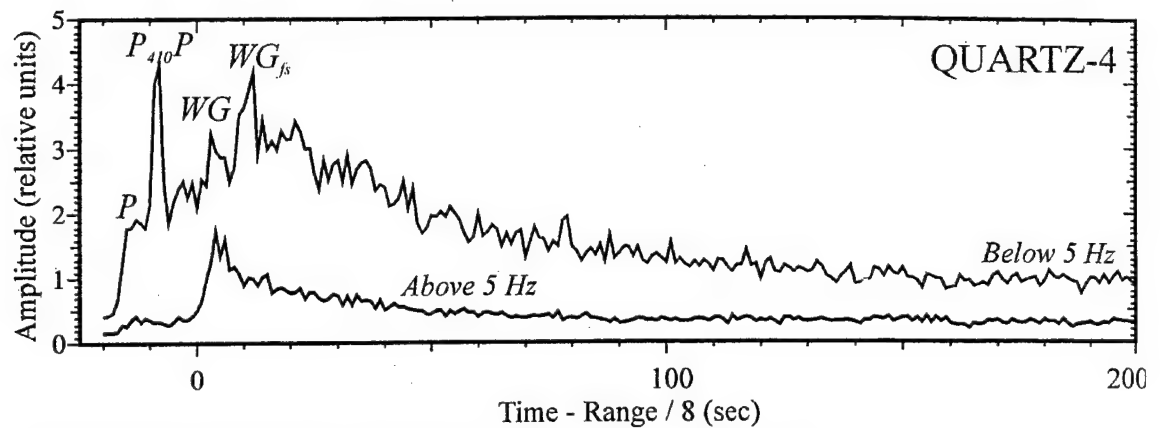
Figure 3. Amplitude of the high-frequency and low-frequency (filter corner frequency is 5 Hz in both cases) records within the offset range 2500 - 2600 km from PNE QUARTZ-4 (modified from Morozov *et al.*, 1998a). Time reduction is 8 km/s, and 7 three-component instantaneous trace amplitude records were averaged within a 2-s sliding time window and within the offset range (Morozov and Smithson, 1996) was used. First arrivals, a reflection from the 410-km discontinuity, and two whispering-gallery phases (WG and WG_{fs}) are indicated. Note the difference of the codas following the free-surface multiple refraction WG_{fs} at low frequencies and the Moho multiple WG at high frequencies.
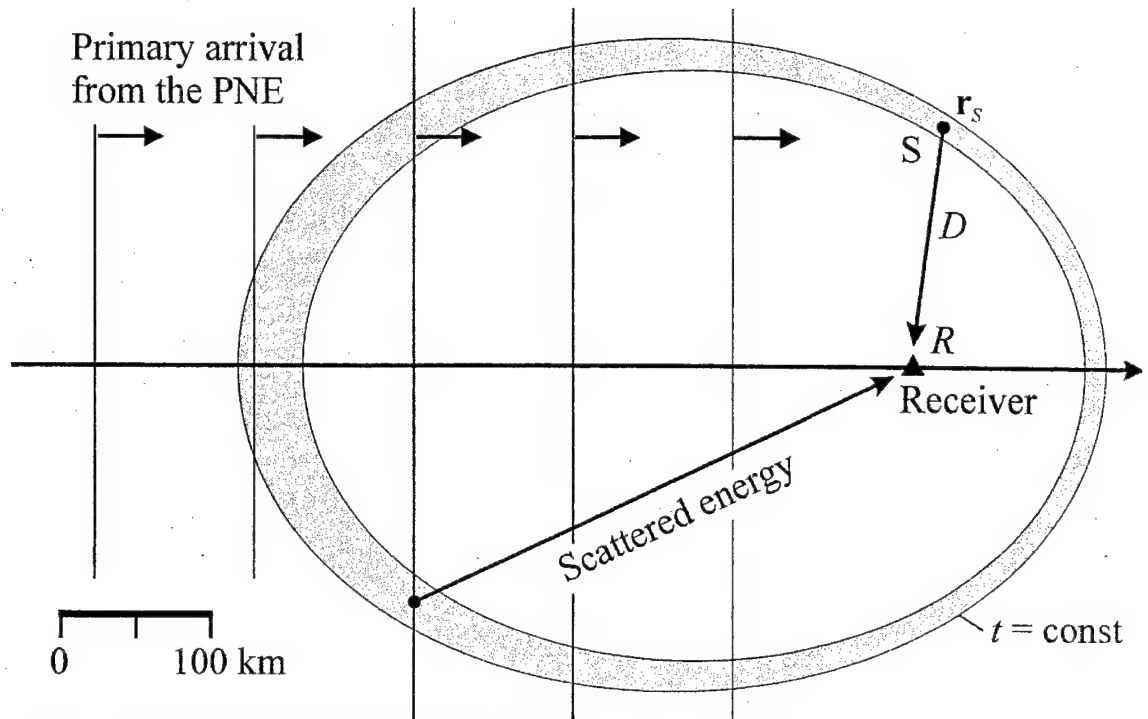
Figure 4. Plan view showing surface area (shaded) of the crust contributing to the coda of the long-range P_n at 50 s after the onset of this phase at the receiver. The PNE is located at 2500 km from the receiver, and the curvature of the incident wavefronts is ignored for simplicity. In this approximation, the scattering area is bounded by two ellipses t = const. Note that an increasing-with-time source area compensates for the geometric spreading of coda energy. For infinite velocity of the primary phase, the scattering area becomes circular, leading to cancellation of geometric spreading in the simplified equation (6). This plot illustrates the notation in integral (5).
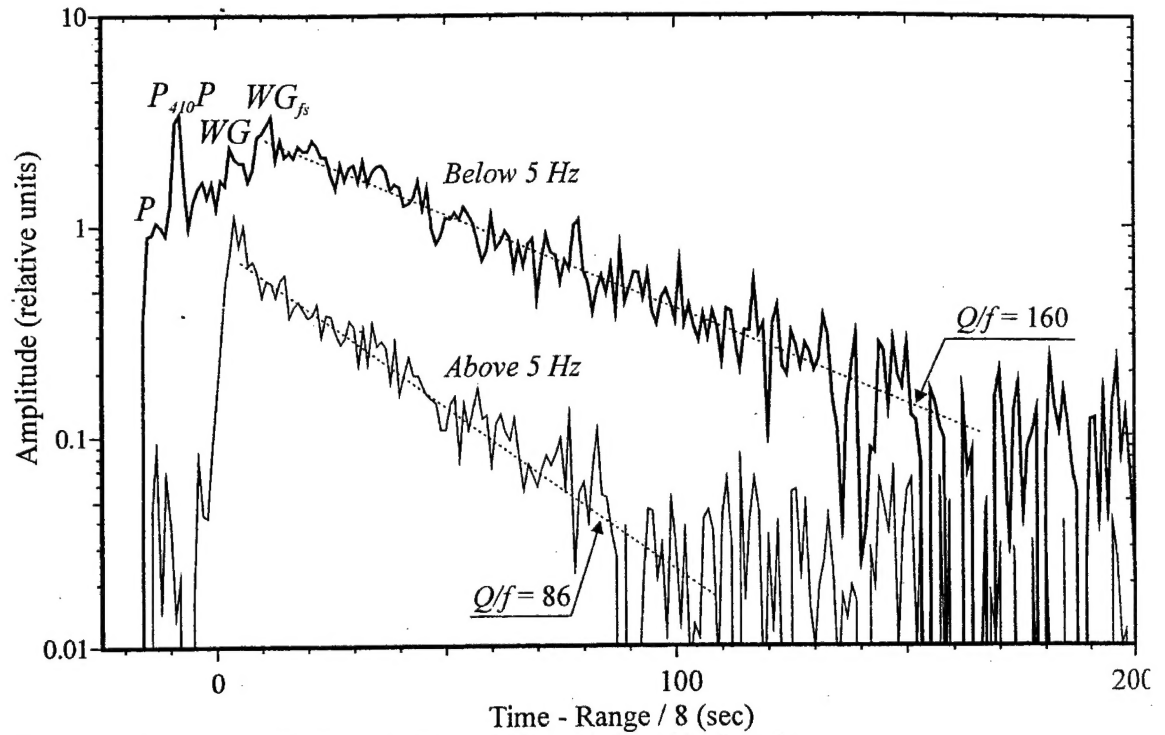
Figure 5. The same amplitudes as in Figure 3 plotted in logarithmic scale. Straight lines correspond to the relation (6) with $Q\approx320$ for the low-frequency curve (at approximately 2 Hz) and $Q\approx430$ for high frequency (at 5 Hz). Background noise estimated from a time window between 300- 350 s of the records was subtracted from both records prior to taking logarithm.
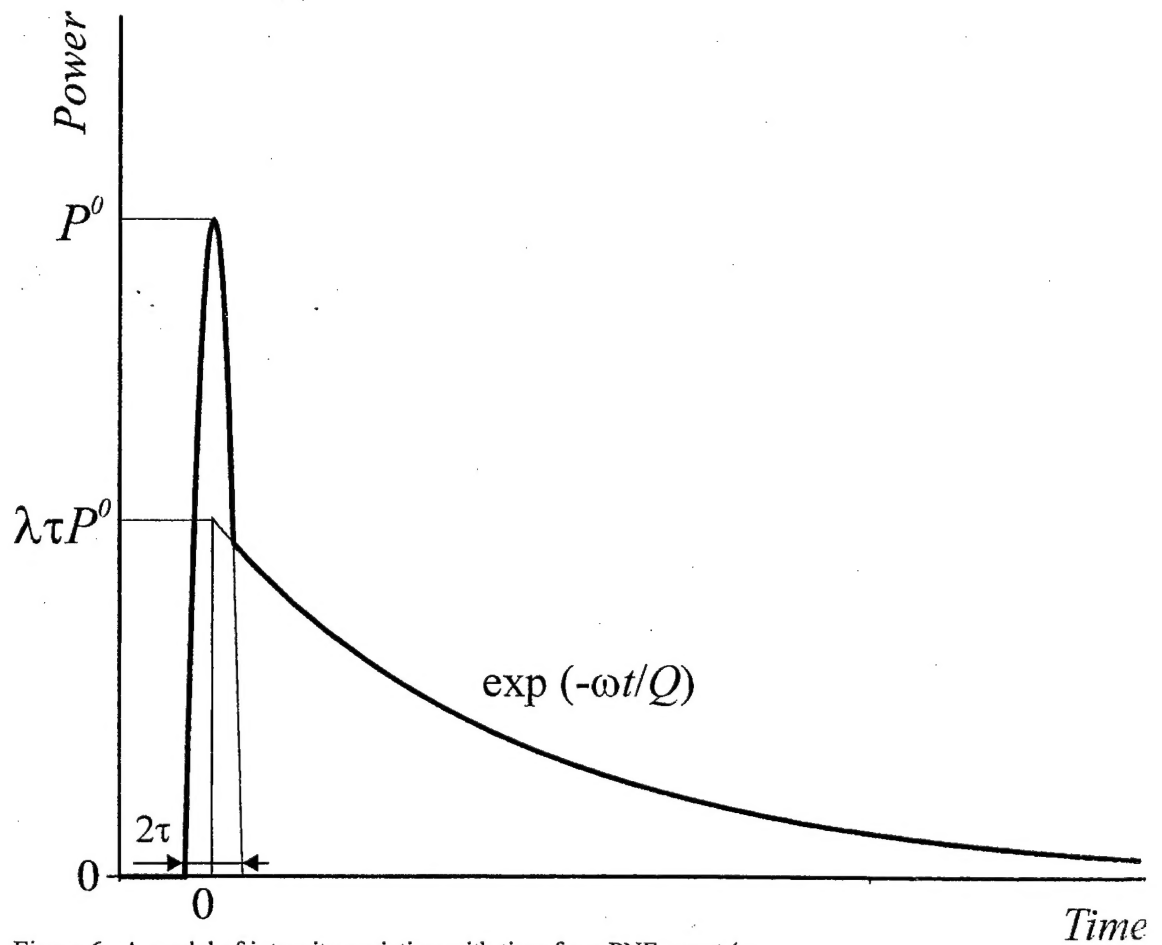
Figure 6. A model of intensity variation with time for a PNE event (see equations (7)). The energy of the primary event is approximated by a parabolic function and is characterized by its peak power P^0 and duration τ. The coda is parameterized by its coupling to the primary event λ and by its decay rate ω/Q defined in relation (6).
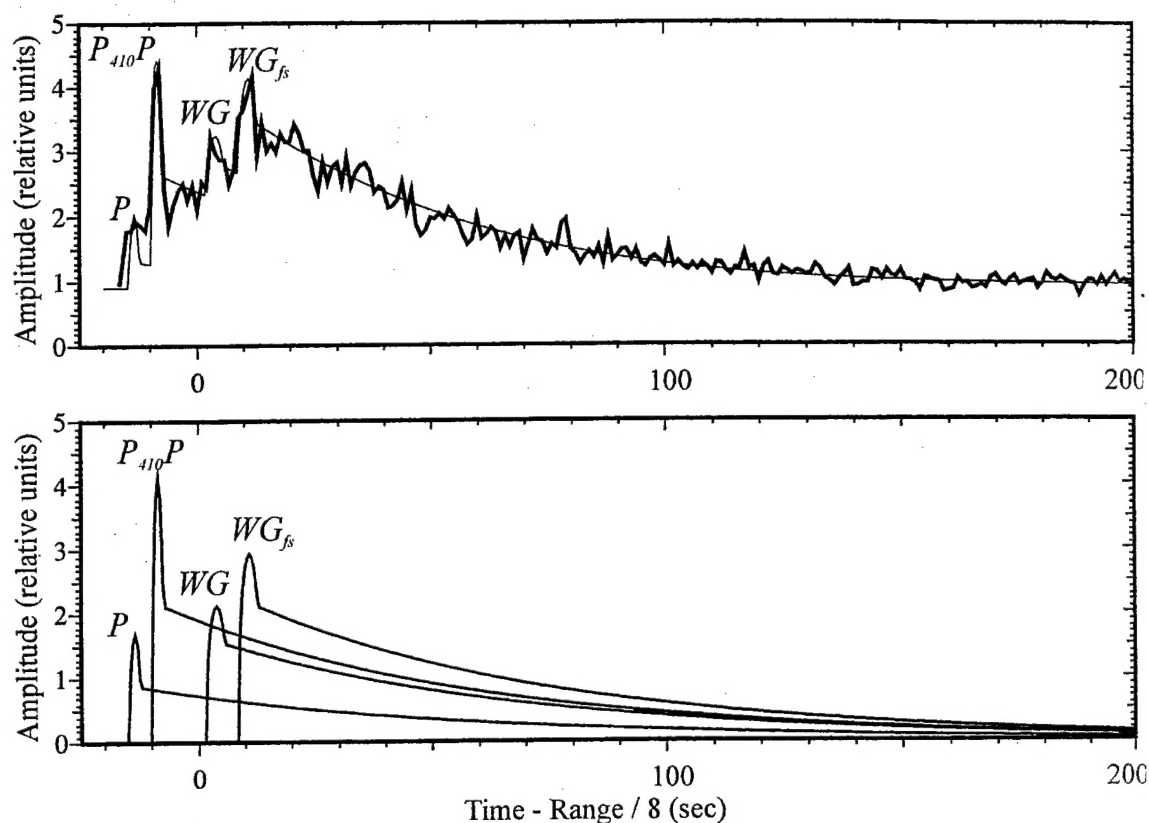
Figure 7. *Top*: Coda amplitude decay model for frequencies below 5 Hz (Figure 3). Thick line is the low-frequency amplitude from Figure 3, thin line shows the modeled amplitude decay described by relation (8). Note that crustal scattering and a simple approximation of coda power (1) explain the observed coda build-up by the subsequent P, $P_{410}P$, WG, and WG_{fs} arrivals. *Bottom*: Amplitudes and codas of the four separate arrivals forming the total coda energy (8). Note that this decomposed section is dominated by the reflection $P_{410}P$. Also compare the amplitude of WG in this plot to the high-frequency WG coda in Figure 3 and note that WG is stronger at lower frequencies, as expected.
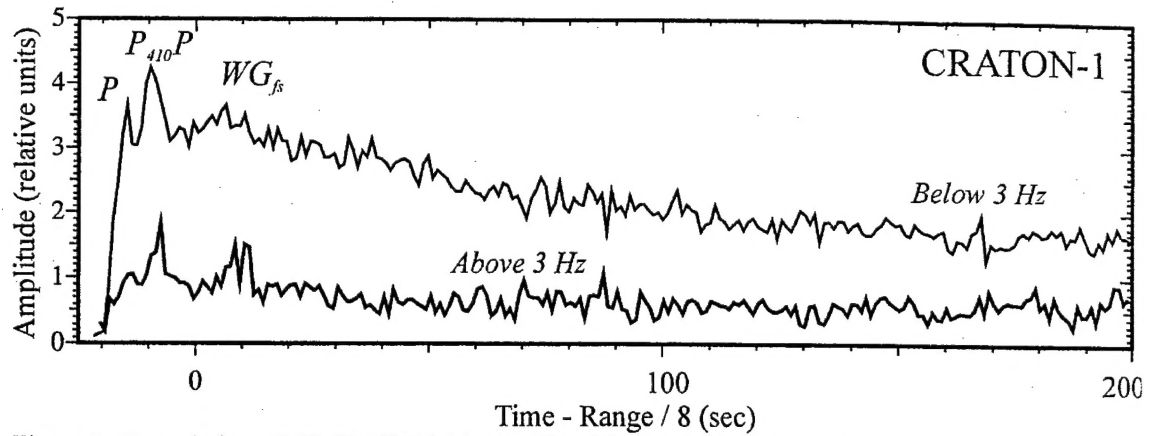
Figure 8. Records from PNE CRATON-1 in the West Siberian basin averaged and plotted in the same way as QUARTZ-4 records in Figure 3. Due to lower frequency content of these records, the frequency band separation is performed at 3 Hz instead of 5 Hz in Figure 3. Note that even without correcting for coda build-up, the WG_{fs} is weaker than $P_{410}P$ and also much weaker than in the records from QUARTZ-4 (Figure 3). Also note the longer codas and increased high-frequency content of WG_{fs} (compared to WG), in contrast to Figure 3. These differences suggest regional variations in WG propagation characteristics and lower crustal attenuation within the Siberian craton.